Global distribution of total ozone on Mars from SPICAM/MEX UV measurements

Séverine Perrier, Jean-Loup Bertaux, Franck Lefèvre, Sébastien Lebonnois, Oleg Korablev, Anna Fedorova, Franck Montmessin

▶ **To cite this version:**

Séverine Perrier, Jean-Loup Bertaux, Franck Lefèvre, Sébastien Lebonnois, Oleg Korablev, et al.. Global distribution of total ozone on Mars from SPICAM/MEX UV measurements. Journal of Geophysical Research, 2006, 111 (E9), pp.E09S06. 10.1029/2006JE002681 . hal-00112447

HAL Id: hal-00112447
https://hal.science/hal-00112447

Submitted on 15 Nov 2020

HAL is a multi-disciplinary open access archive for the deposit and dissemination of scientific research documents, whether they are published or not. The documents may come from teaching and research institutions in France or abroad, or from public or private research centers.

L'archive ouverte pluridisciplinaire **HAL**, est destinée au dépôt et à la diffusion de documents scientifiques de niveau recherche, publiés ou non, émanant des établissements d'enseignement et de recherche français ou étrangers, des laboratoires publics ou privés.

Global distribution of total ozone on Mars from SPICAM/MEX UV measurements

S. Perrier,[1] J. L. Bertaux,[1] F. Lefèvre,[1] S. Lebonnois,[2] O. Korablev,[3] A. Fedorova,[3] and F. Montmessin[1]

Received 22 January 2006; revised 14 June 2006; accepted 12 July 2006; published 27 September 2006.

[1] The dual UV/IR spectrometer SPICAM on board the European mission Mars Express is dedicated to monitoring the Martian atmosphere and has recorded spectra for more than one Martian year, from January 2004 to April 2006, over a large range of latitudes and longitudes. SPICAM UV spectra were recorded on the day side in a nadir geometry, in the 110–320 nm range, allowing measurement of ozone absorption around 250 nm. The method used to retrieve column-integrated ozone quantities is described. A full radiative transfer forward model of the radiance factor is used in an iterative loop to fit the data with four parameters: the surface albedo at 210 and 300 nm, the dust opacity, and the total ozone column. The analysis of the complete data set is presented. The global climatology of ozone on Mars is retrieved for the first time with spatial and temporal coverage. The most significant findings are (1) large increases in the ozone column density at high latitudes during late winter-early spring of each hemisphere that totally disappear during summer, (2) a large variability of the northern spring content related to the polar vortex oscillations, (3) low ozone columns in the equatorial regions all year long, and (4) local variations of the ozone column related to topography, mainly above Hellas Planitia. A good overall agreement is obtained comparing SPICAM data to predictions of a Chemical General Circulation Model. However, significant discrepancies in total abundances are found near northern spring when ozone reaches its annual peak. These results will help further understanding of the dynamics and chemistry of Mars atmosphere.

Citation: Perrier, S., J. L. Bertaux, F. Lefèvre, S. Lebonnois, O. Korablev, A. Fedorova, and F. Montmessin (2006), Global distribution of total ozone on Mars from SPICAM/MEX UV measurements, *J. Geophys. Res.*, *111*, E09S06, doi:10.1029/2006JE002681.

1. Introduction

[2] Ozone is one of the most important, and one of the most reactive species in the Martian atmosphere. It controls the UV flux that reaches the ground, thus the habitability of the planet. It also traces HO_x radicals (H, OH, and HO_2), that are responsible for the stability of the atmosphere (recycling CO_2 molecules photodissociated in the upper atmosphere). Thus understanding the distribution and variability of ozone is related to more general problems concerning the Martian atmosphere.

[3] The local concentration of ozone depends on the abundance of odd hydrogen species (HO_x) produced by the photo-dissociation of water vapor. However, HO_x radicals have never been directly observed. Their abundance has to be derived through modeling from the amount of water vapor, which largely depends on latitude and season [*Smith*, 2002]. Alternatively, ozone (O_3), which is formed by the three-body reaction of O and O_2 and is destroyed by HO_x, can be used as a tracer of these odd hydrogen radicals. Moreover, the comparison between ozone measurements and model predictions can highly improve our understanding of the Martian atmosphere's photochemistry.

[4] Ozone on Mars was first detected by the UV spectrometers aboard Mariner 7 and Mariner 9 in 1969 and 1971–72, respectively [*Barth and Hord*, 1971; *Barth et al.*, 1973; *Wherbein et al.*, 1979]. A few ozone measurements were performed by the Russian missions Mars 5 and Phobos 2 [*Krasnopolsky and Parshev*, 1979; *Blamont and Chassefière*, 1993]. UV observations, which have to be made outside Earth's atmosphere, were also performed with the Faint Object Spectrograph from Hubble Space Telescope (HST-FOS) [*Clancy et al.*, 1996a, 1999].

[5] Two other ozone probing methods are possible from the Earth's surface, in the infrared. One is to measure the intensity of the $O_2(^1\Delta)$ 1.27 μm dayglow emission of O_2, which is a good tracer of ozone abundance above 20 km altitude [*Noxon et al.*, 1976; *Novak et al.*, 2002; *Krasnopolsky*, 2003]. The other way is infrared heterodyne spectroscopy which directly measures Martian ozone absorption from the

[1] Université de Versailles Saint-Quentin-UVSQ, Service d'Aéronomie du CNRS/IPSL, CNRS/UVSQ/UPMC, Verrières-le-Buisson, France.
[2] Laboratoire de Météorologie Dynamique, CNRS/UPMC/IPSL, Paris, France.
[3] Space Research Institute (IKI), Moscow, Russia.

Copyright 2006 by the American Geophysical Union.
0148-0227/06/2006JE002681

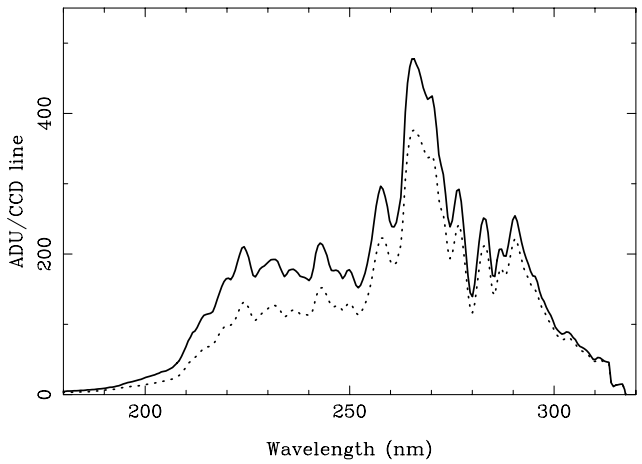

Figure 1. Example of two SPICAM spectra in ADU (Analog to Digital Unit) for orbit 1448 (4 March 2005, L_s = 170°). These spectra were averaged over 20 s. The solid line is the spectrum at the foot of the Olympus Mons volcano; the dotted line is the spectrum above the summit of the volcano. The spectral shape is mainly dictated by the solar flux (see Figure 3) and the spectral sensitivity of the instrument. The difference between these two spectra is mainly due to more Rayleigh scattering at lower altitude.

surface of the Earth in the 9.6 micron band [*Espenak et al.*, 1991; *Fast et al.*, 2006].

[6] This paper presents the ozone total column densities derived from SPICAM nadir UV spectra, collected over more than one Martian year. The Mars Express mission started to observe the red planet in January 2004, at a solar longitude L_s = 331°, where L_s is the orbital position relative to 0° at the northern spring equinox. Observations were performed during one full Martian year (Mars Year MY27, according to the numbering scheme set by *Clancy et al.* [2000]) and Mars Express is now continuing the measurements for the second Martian year. Data presented here have been collected up to L_s = 37° of MY28. These data represent the most comprehensive data set on ozone in the Martian atmosphere.

[7] We first describe briefly the SPICAM instrument and the characteristics of the data used in this study. In section 3 we detail the method used to retrieve ozone quantities from spectra. Complete analysis of the nadir-viewing spectra obtained with SPICAM season by season is presented in section 4. Interannual comparisons and comparisons with other available O_3 measurements are also shown. Discussion and some comparisons with GCM predictions are presented in section 5. Our conclusions are presented in section 6.

2. UV Nadir Observations With the SPICAM/MEX Instrument

2.1. SPICAM Instrument Description and Mode of Operation

[8] SPICAM is a 4.7 kg UV-IR instrument on board the European Mars Express mission launched in June 2003. The orbiter has an elliptical polar orbit with a period of about 7 hours, a pericenter altitude of ≃300 km and apocenter altitude of ≃10000 km. SPICAM is mainly dedicated to the determination of atmospheric characteristics of Mars from the ground up to 160 km altitude, and ozone mapping is one of its major scientific objectives. The scientific objectives were presented by *Bertaux et al.* [2000], and a more complete description of the instrument is given by *Bertaux et al.* [2006]. In this paper, we focus on observations made with the UV spectrometer which observes in the range 115–310 nm. The spectral resolution per pixel ($\delta\lambda$) is about 1 nm, and the resolving power $R = \lambda/\delta\lambda$ is 120–300.

[9] To measure O_3 total column densities, nadir observations were performed: SPICAM observes Mars through its atmosphere with a line of sight perpendicular to the ground (nadir). In some limited cases (3%), the line of sight has been inclined by up to 30 degrees (the so-called emission angle ξ) for the needs of other instruments aboard MEX.

[10] The typical duration of nadir observations is 30 min. In nadir viewing mode, the spectral radiance is recorded each second, with an integration time of either 320 or 450 ms (chosen to avoid saturation). The main nadir collecting mode is to read the CCD by binning 4 lines together (on chip) in 5 contiguous bins, providing 5 spectra each second. Averaging these 5 spectra provides an averaged spectrum that is used to retrieve the ozone column density. This spectrum corresponds to 20 lines of the CCD and a typical field of view (FOV) of 1.2 × 2.4 km at pericenter. These raw data were averaged over 50 s (i.e., 50 successive spectra), to improve the signal-to-noise ratio and reduce the analysis computing time (see section 3): each nadir observation finally provides 30 to 40 independent averaged spectra to be analyzed for ozone retrieval.

[11] All the data analyzed in this paper have been collected during more than one Martian year of observations, from January 2004 to April 2006. This corresponds to 1083 nadir observations from orbit number 8 (9 January 2004, solar longitude L_s = 331°) to orbit number 2882 (9 April 2006, L_s = 37°), providing around 28,000 high-S/N spectra.

2.2. Data Description

[12] Raw data are expressed in ADU (Analog to Digital Unit). They must be corrected for offset (added to avoid negative values at the entry of the A/D converter) and dark current pixel to pixel nonuniformity (DCNU, derived from nadir observations at night). A stray light correction is applied to all nadir data, from the study of the limb observation during orbit 1788 (realized in June 2005 with a special position of the slit of the detector). The method is explained in detail by *Bertaux et al.* [2006]. For the correction of the nadir data, we assume that the observed scene is uniform over the whole slit at each second. If there are large changes on the ground at a scale of a few kilometers (as it is the case over polar caps), the correction of the stray light might be less accurate. An example of raw data and corrected data (average over the pixels, as a function of time) is given in Figure 18 from *Bertaux et al.* [2006]. The amount of stray light is about 8–12% of the total signal.

[13] Figure 1 shows an example of two corrected SPICAM spectra. These spectra were averaged over 20 s, i.e., averaged over one hundred individual spectra. Note in Figure 1 that the signal intensity largely decreases at wave-

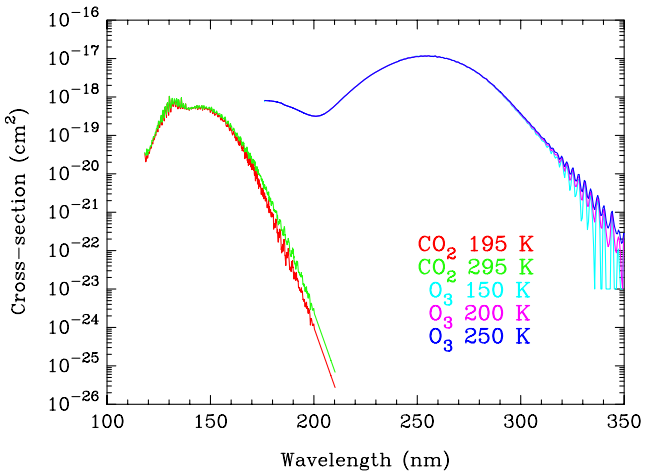

Figure 2. Absorption cross sections of CO_2 and O_3 molecules (cm^2) in the 120–350 nm spectral range, at various temperatures.

lengths shorter than 210 nm, due to the combined effects of dramatic decrease of solar flux (see Figure 3) and strong absorption by CO_2 molecules in the Martian atmosphere at these wavelengths. On the other end of the spectra, the decrease of detector sensitivity limits the study to wavelengths shorter than 300 nm.

3. Data Analysis: Method for Ozone Retrieval

[14] Radiance measured by SPICAM in a nadir-viewing geometry corresponds to the solar light scattered by surface, CO_2 molecules, dust and clouds, and not absorbed by ozone or CO_2. Because the contributions of different factors combine to form the final observed quantity (spectral radiance I or radiance factor I/F, see definition in section 3.3), it is not easy to disentangle the relative contributions of scattering of atmospheric components and surface scattering (albedo).

3.1. UV Gaseous Absorption and Solar Spectrum

[15] Absorption cross sections of CO_2 and O_3 molecules are shown in Figure 2. This plot shows that in the range 210–300 nm, CO_2 absorption can be neglected. The total vertical column of O_3 is determined from the ozone absorption in the Hartley band (220–280 nm), imprinted on the backscattered solar radiation. This absorption feature is very broad($\Delta\lambda \simeq 40$ nm) (see Figure 2). Ozone absorption is maximum around 255 nm. Rayleigh scattering and aerosol absorption/scattering are to be accounted for, besides the extinction by ozone.

[16] Figure 3 shows, for the UV spectral range of SPICAM, the solar flux at 1 AU (in photons/cm^2/s/nm), as measured by SOLSPEC experiment [*Thuillier et al.*, 2003]. The spectral sensitivity of SPICAM is given in *Bertaux et al.* [2006].

3.2. Possible Methods for Ozone Column Retrieval

[17] On the two planets Earth and Mars, the solar back scattered UV radiation can be analyzed from space to estimate the total vertical content of ozone (in short, total ozone). On Earth, it has proved to be an excellent method, with retrieval methods developed over 4 decades, and requiring the measurement of absolute radiance at only two wavelengths by the TOMS series of instruments [*Dave and Mateer*, 1967; *Bhartia et al.*, 1996]: at 331.2 nm to estimate an effective surface reflectivity or cloud fraction, and at 317.5 nm, more sensitive to ozone, with an implicit assumption that the reflectivity has no significant variation between the two wavelengths. Four other UV wavelengths are used for quality control and treat some special situations [*Bhartia et al.*, 1996].

[18] Though in principle the situation of UV radiation on Earth and Mars are apparently similar, there are great differences between the two planets that makes the elegant solutions established for TOMS and now OMI (Ozone Monitoring Instrument) not directly applicable to the retrieval of total ozone on Mars. First, the total ozone of Mars (though highly variable) is ~200 times less than on Earth: a typical large amount of ozone on Mars is 15 μm-atm (1 μm-atm = $2.69.10^{15}$ molecules.cm^{-2} = 0.1 Dobson Unit or DU), while on Earth it is rather 300 DU. Even at its wavelength of maximum cross section (at 255 nm, $\sigma = 1.175.10^{-17}$ cm^2), the optical thickness is only 0.47 for 15 μm-atm (and 0.32 for 10 μm-atm): the Hartley band is not saturated, and the radiation reaches the ground at all UV wavelengths greater than 200 nm (above the cut-off of CO_2 absorption, Figure 2). Therefore, on Mars, the whole Hartley ozone absorption band can be used.

[19] While on Earth aerosols are confined near the ground, well below the ozone layer, on Mars dust is abundant, highly variable (with a variable optical thickness 0.1–1), and extends at high altitudes, intimately mixed with ozone. It is therefore not possible to assume, like in the TOMS retrieval, that the aerosols contribution to the emerging radiance may be included in the surface reflectivity [*Bhartia and Wellemeyer*, 2002]. The vertical distribution is also quite different. On Earth, the bulk of total ozone is concentrated in the single stratospheric layer, essentially above the UV radiation scatterers. On Mars, there are two distinct ozone layers with significant contributions to total

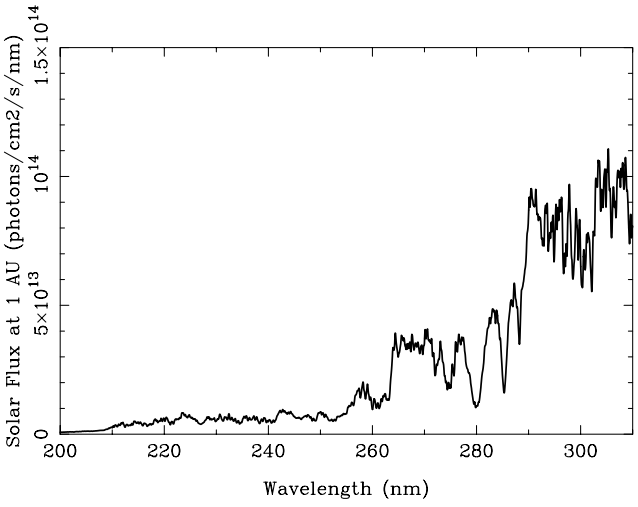

Figure 3. Solar spectrum (photons/cm^2/s/nm) at 1 AU from the SOLSPEC experiment [*Thuillier et al.*, 2003].

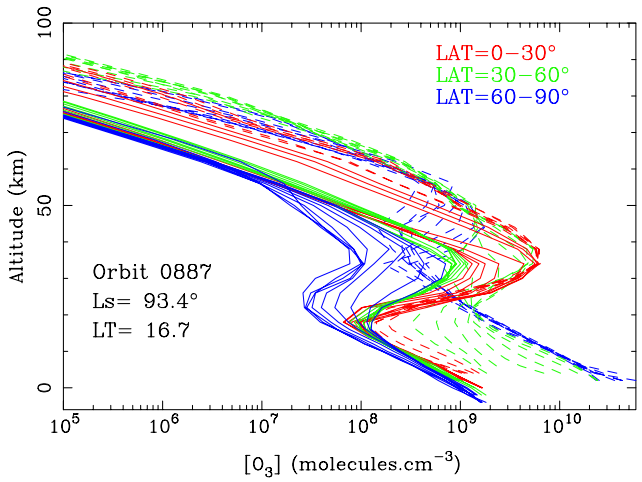

Figure 4. Ozone vertical profiles predicted by GCM at different latitudes. Solid lines are for northern latitudes, and dashed lines are for southern latitudes. These profiles were computed for conditions of observation relative to orbit 887, $L_s = 93.4°$, local time 16.7. At variance with the case of the Earth where the shape of the profile is rather constant, there is a variety of vertical profiles, even on one particular day. In particular, the maximum concentration is either at the ground or in the range 30–50 km.

ozone, as shown in Figure 4: a high-altitude layer, and a low-altitude layer, which contribution is strongly modulated by topography (the surface altitude changes from −6 km to +14 km).

[20] We first tested a very basic method, in which only three points per spectrum are considered: (1) two points outside the O_3 absorption band, at 210 and 300 nm (related intensities are called I_1 and I_2, respectively), and (2) one point at the ozone absorption peak (255 nm), where the observed intensity is I_o. The Beer-Lambert law was used to retrieve ozone column $I_o = I_w \cdot \exp(-M \cdot N_{O_3} \cdot \sigma_{O_3})$ where I_w is the intensity that would be observed at 255 nm without ozone, inferred by linear interpolation between I_1 and I_2. M is the air mass factor, σ_{O_3} is the ozone absorption cross section at 255 nm and N_{O_3} is the wanted parameter, the total ozone column. This method is efficient detecting the presence of ozone but gives a poor estimate of the column densities, with typical errors of 50% or more.

[21] The second method is more elaborate. It uses a detailed forward model of the atmosphere and takes into account the specific geometry of each observation (ground altitude, solar zenith angle, emission angle). Assumptions (a priori information) have to be made on several parameters: surface pressure, temperature profile, and ozone relative vertical profile. The best guess is to take the results from GCM computations. The ozone column density is a free parameter of the model, as well as the ground albedo. The model computes the spectra, including Rayleigh scattering, absorption by ozone, and assuming that the atmosphere is dust-free in a first step. A least-squares fitting algorithm is used to adjust the modeled spectrum to the observed one, and hence to estimate the ozone column density (and surface albedo). A third method, which was finally adopted for a systematic treatment of all orbits, is similar to method 2 but accounts for the possible presence of dust in the atmosphere. Fixed assumptions are made on the optical properties and distribution, but the dust opacity is a free parameter. This third method is computationnally slower than method 2 (around four times), and requires a long computation time. We used the results of method 2 to study the influence of dust on our results (see section 3.5).

3.3. Radiative Transfer Forward Model

[22] To simulate ultraviolet spectra observed by SPICAM, we developed a forward model using the radiative transfer code SHDOM (Spherical Harmonic Discrete Ordinate Method) [*Evans*, 1998] in a plane-parallel atmosphere. The output of this forward model is the radiance factor I/F, computed separately at various wavelengths within the 210–300 nm range. Here, I is the intensity brightness of the target, and πF is the solar flux at the top of atmosphere at the particular wavelength. The atmosphere is modeled from the ground to 60 km by twelve 5 km-thick layers. The exact geometry corresponding to each averaged spectrum to be fitted (SZA, emission angle, phase angle) is taken into account. The maximum size of one averaged spectrum on the ground is 1.2 km × 250 km (at pericenter). All the spectra collected at a solar zenith angle greater than 85° are not considered for fitting.

[23] The ground albedo is described by two parameters: its values at 210 and 300 nm, and a linear behavior is assumed in the 210–300 nm range. The emission scattering from ground is assumed to be Lambertian. The surface pressure is taken from the Martian GCM of *Forget et al.* [1999], and the density of the atmosphere at the altitude of each layer is deduced from the hydrostatic equilibrium. The temperature profile is taken from GCM predictions at the local time, longitude and season of the observation. To compute the gaseous absorption, we use the most recent absorption cross sections. At wavelengths larger than 210 nm, absorption by CO_2 molecules is negligible [*Parkinson et al.*, 2003]. Ozone is represented by one single free parameter in the model, its vertically integrated column density. The vertical distribution of ozone is assumed to be proportional to that predicted by the GCM coupled to a chemistry module of *Lefèvre et al.* [2004] at the same time and place. Some examples of profiles (around $L_s = 90°$) are given in Figure 4. Note that at equator and low latitudes, ozone is present in a layer of 30–50 km high, whereas at high latitudes ozone is more concentrated near the surface. The O_3 cross sections are from *World Meteorological Organization* [1986], recommended by *Sander et al.* [2003], and include the temperature dependent measurements from *Molina and Molina* [1986]. The model computes the effect of Rayleigh scattering of the atmosphere, and of pure absorption of gases (CO_2 and ozone). In addition, dust scattering and absorption were included in the radiative transfer model. The vertical distribution for dust was taken following the formula proposed by *Conrath* [1975]:

$$q(z) = q_0 \cdot e^{\gamma \cdot \left(1 - \exp\left(\frac{z}{H}\right)\right)} \quad (1)$$

where q is the dust extinction coefficient at a certain altitude (q_0 for the dust extinction at the ground) and γ is the

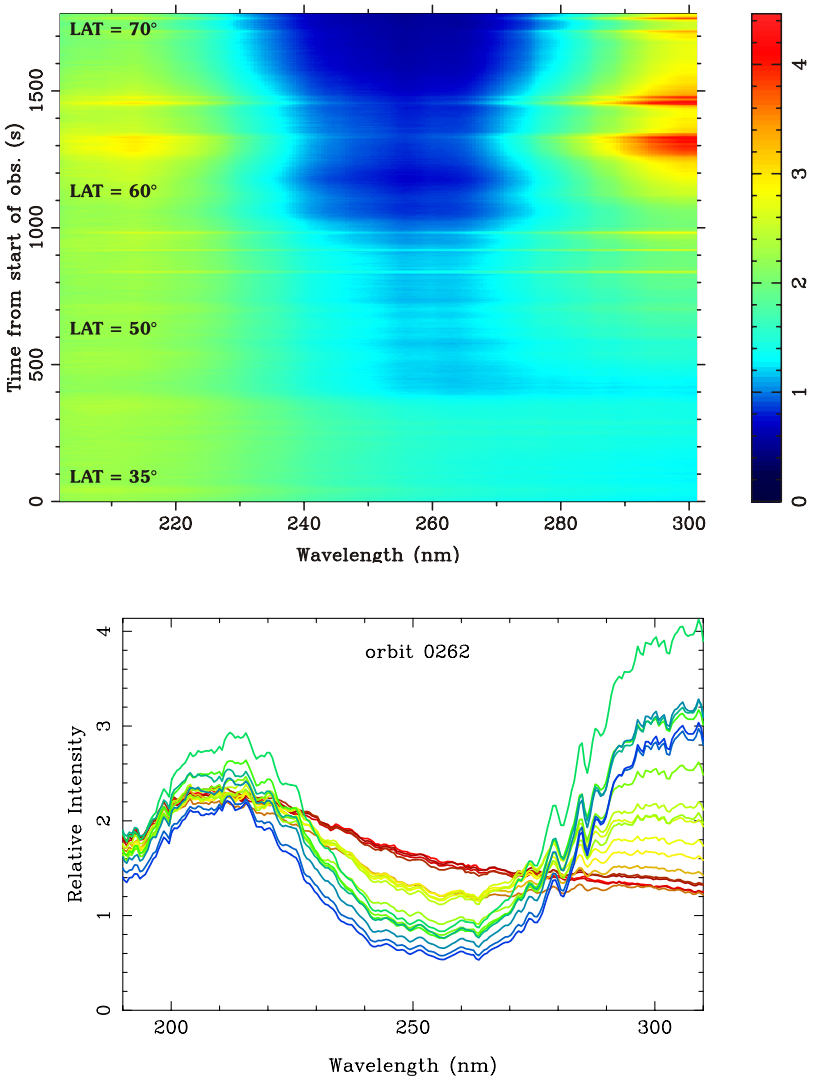

Figure 5. (top) Spectrotemporal image recorded during orbit 262, on 1 April 2004 (L_s = 13.3°). The x axis is the wavelength, and the y axis is time (seconds). The color code represents the relative intensity (all spectra were divided by the same Data Reference Spectrum recorded above Olympus Mons). This observation begins from equatorial latitudes and moves toward the north pole. Ozone absorption around 255 nm is visible at high latitudes. Note the strong intensity variations around time from 1200 to 1500 s, possibly due to icy ground. (bottom) Example of relative spectra: spectra of orbit 262 divided by the Data Reference Spectrum above Olympus Mons. The color code indicates the latitude variation (red for the equator, blue for polar latitudes). The data have not been smoothed in wavelength in this picture. For ozone retrieval, the spectra are smoothed over 10 pixels (5 nm). Small wiggles around 280 nm are spurious (nonperfect wavelength registration).

Conrath parameter (the higher γ, the shallower the dust layer). We adopted the value of 0.03 which is thought to represent typical dust conditions on Mars [*Pollack et al.*, 1990]. To specify physical properties of dust, we had to choose values for single scattering albedo ω and the asymmetry parameter g. These parameters are very poorly constrained in the UV. For simplicity, we have assumed ω and g to be invariant over the 210–300 nm spectral range. We adopted the value of 0.6 for ω, which was also adopted by *Clancy et al.* [1999] after the analysis of the HST image of a Valles Marineris dust storm in 1997. Dust scattering phase function is represented by a Henyey-Greenstein function, which solely depends on the asymmetry parameter g. The value of 0.88 was adopted for g, following the value given by *Ockert-Bell and Bell* [1997] at 300 nm.

3.4. Method for Ozone Retrieval in SPICAM UV Spectra

3.4.1. Relative Method

[24] For each observation, we divide each recorded spectrum by a particular SPICAM spectrum, called Data Reference Spectrum (DRS). One advantage of this "relative" method is to avoid the issue of the instrument absolute calibration. Moreover, this method does not require an

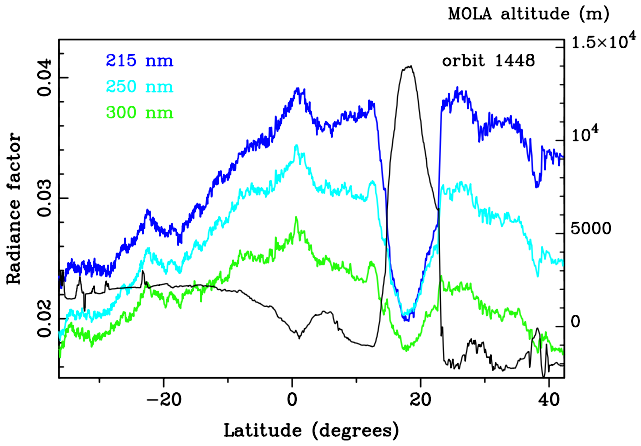

Figure 6. Radiance factor as a function of latitude, for orbit 1448 (on 4 March 2005, L_s = 170°), for three wavelengths at 210 nm, 250 nm, and 300 nm in dark blue, light blue, and green, respectively. In black, the MOLA (Mars Orbiter Laser Altimeter) altitude of the ground. The altitude peak centered on LAT = 18°N is Olympus Mons. Above the volcano, the atmosphere is very tenuous (P_0 = 1.8 mbar at the summit), so Rayleigh scattering is much weaker than at the foot of the mountain, leading to a decrease in the radiance factor. This effect is more pronounced at shorter wavelength, as expected with Rayleigh scattering (in λ^{-4}).

accurate knowledge of the spectrometer resolution (about 1.5 nm), which is a crucial point when a simulated solar spectrum is needed. Figure 5 shows the relative spectra obtained during observation of 1 April 2004 (orbit 262) at early spring (L_s = 13.3°), as a function of latitude. The field of view is moving from low latitudes of northern hemisphere to high latitudes. Ozone absorption is increasing at high latitudes. The latitude drift during this observation varies from 33°N to 70°N, and the SZA from 30° to 65°. The longitude of the observation is −10° (East longitudes). In Figure 5 (bottom), only every other averaged spectrum is plotted. The color code corresponds to the latitude. The fine-scale wavelength structures are not due to atmospheric components (Hartley band ozone is broad and featureless at the resolution of the instrument) but possibly to some residual instrumental effects (i.e., small variations in wavelength assignment) or small variations in surface albedo. These spectra are smoothed over 10 pixels (5 nm) during the ozone retrieval process.

[25] In order to model these relative spectra, which contain a mixture of contributions of dust, ozone, aerosols and variable ground albedo, we need to have a complete modeling of the data reference spectrum.

3.4.2. Data Reference Spectrum (DRS)

[26] We built a Data Reference Spectrum (DRS) corresponding to an ozone-free atmosphere, with a minimal amount of dust and aerosols. These conditions are assumed to be met above the highest volcano, Olympus Mons. The DRS has then been defined as the average of the spectra recorded above Olympus Mons during orbit 1448 (on 4 March 2005, L_s = 170°), near the top of the volcano (spectrum shown in Figure 1). Above the Olympus Mons volcano (centered around 18°N), the surface pressure strongly decreases, which implies a severe decrease of the Rayleigh scattering and thus a decrease in the UV signal. The decrease is shown in Figure 1 and also in Figure 6, showing the radiance factors at 210 nm, 250 nm and 300 nm as a function of latitude. The decrease of the signal is relatively stronger at 210 nm than at 250 nm and then at 300 nm, which is consistent with a decrease of the Rayleigh scattering, itself due to a severe decrease of the atmospheric mass (the surface pressure is 1.9 mbar at the top while it is 6 mbar at the foot of the volcano). We assume that this spectrum is affected neither by ozone, as confirmed by GCM predictions (GCM value of ozone column density above Olympus Mons is 0.12 μm-atm for this observation) nor by dust, assumed to be negligible at this elevation. It only contains the effects of atmospheric Rayleigh scattering and extinction, which are exactly computed, and the reflection by the surface (which can therefore be easily retrieved).

[27] The wavelength dependence of the Martian surface albedo is poorly known over the 210–300 nm wavelength range. A method to derive the surface albedo is to study observations during which large topographic variations are observed, leading to large variations of the surface pressure. This is the case in particular above Olympus Mons. The spectra were averaged over 20 s, in order to increase the signal-to-noise ratio. Raw data were converted to radiance factor $R = I/F$ using an adequate absolute calibration (efficient area of the detector determined by stellar occultations technique [see *Bertaux et al.*, 2006, Figure 11]), I being the actual radiance received from Mars within each SPICAM pixel and F the theoretical radiance received within each SPICAM pixel from a perfectly scattering Lambertian surface illuminated by the Sun (flux πF) and

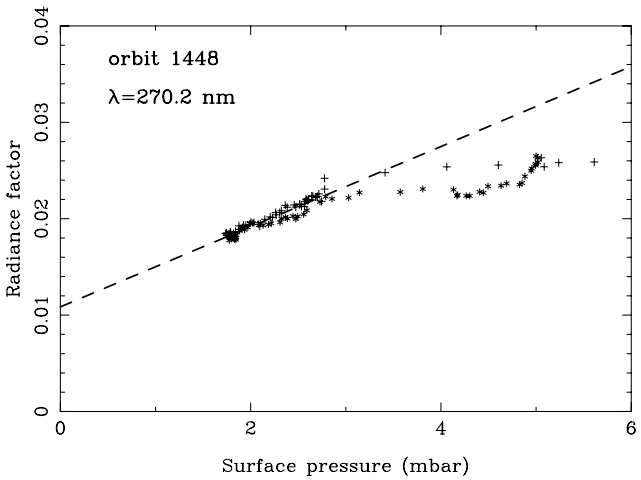

Figure 7. Radiance factor I/F above Olympus Mons as a function of the surface pressure (from GCM), at λ = 270 nm, for orbit 1448 (4 March 2005, L_s = 170°); crosses for data north of O.M., stars for data south of O.M. The dashed line is a linear fit of the low-pressure data. When data are extrapolated down to zero, it gives the actual surface albedo multiplied by cos(SZA), here 0.011. For this observation, SZA above Olympus Mons is equal to 22°. The absolute calibration of the instrument was obtained by observations of stars [*Bertaux et al.*, 2006].

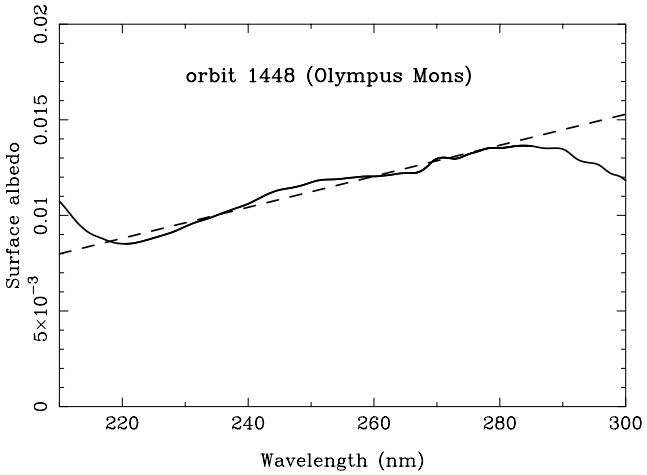

Figure 8. The surface albedo (solid line) of Olympus Mons as a function of wavelength was obtained by extrapolations to zero pressure. The dashed line is a linear fit of the albedo over the [210–300] nm range.

viewed at normal geometry. The radiance factor is plotted versus the surface pressure predicted by the GCM [*Forget et al.*, 1999] in Figure 7 for a given wavelength. Around the summit, at low pressure, the data points show a linear behavior that supports the hypothesis of a rather constant ground albedo. A linear extrapolation from these points down to zero surface pressure gives a value corresponding to the radiance factor in a no-atmosphere case, i.e., surface albedo multiplied by the cosine of the solar zenith angle (SZA).

[28] The same method has been used for each wavelength (Figure 8). The retrieved values of the ground albedo are very low, confirming the already well known extreme darkness of the Martian ground in the UV. The surface albedo variation with wavelength can be considered as linear in a first approximation and represented in the modeling by only two parameters, its value at 210 nm and 300 nm. The retrieved value is 0.008 at 210 nm, and 0.015 at 300 nm. *Clancy et al.* [1999] adopted a wavelength-independent surface albedo of 0.015 for the 220 to 330 nm range of wavelengths. In the past, they used a wavelength-dependant decrease of the ultraviolet albedo (0.015 at 330 nm to 0.010 at 200 nm [*James et al.*, 1994; *Clancy et al.*, 1996b]) which is very similar to our retrieved values.

3.4.3. Model Reference Spectrum (MRS)

[29] Since the data to be fitted consist of relative spectra (measured spectra divided by the Data Reference Spectrum), the model must also provide a corresponding relative spectrum. A Model Reference Spectrum (MRS) was therefore built, with a surface albedo defined by the linear fit of Figure 8. The MRS uses the full radiative transfer model, without dust, but with Rayleigh scattering and extinction, and the particular geometry (SZA and distance to the sun) of the Olympus Mons observations. DRS and MRS are represented in Figure 9. The model relative spectrum to be compared to data is obtained from the model absolute spectrum (radiance factor) computed at each point, divided by MRS.

3.4.4. Fitting Method

[30] We use a Levenberg-Marquardt fitting method (least square minimization method) from Numerical Recipes. A first analysis of the data was made with three free parameters (all forced to be positive): ground albedo at 210 nm and at 300 nm and ozone column density, assuming there is no dust in the atmosphere. A second analysis was then performed by adding a fourth free parameter: the dust opacity in the atmosphere. All free parameters are forced to remain positive. As mentioned earlier, dust scattering in the atmosphere is described by Henyey-Greenstein phase function with an asymmetry parameter g equal to 0.88 and a single scattering albedo ω equal to 0.6 for all wavelengths. The dust opacity is also assumed to be independent of wavelength. The value returned by the fit is scaled to the Mars reference pressure of 6.1 mbar, since it is often assumed that dust is well mixed in the atmosphere, and in order to avoid local topographic effects. In our study, we do not account for the possible presence of clouds.

[31] The data are fitted between 220 and 300 nm, and 9 averaged spectral points are used (one every 10 nm). Along one orbit, all averaged spectra (over 50 s) are fitted independently from each other. Figure 10 shows two examples of fits for orbit 262, at two different latitudes, 41°N and 60°N. At 41°N, the retrieved ozone column density is 2.6 μm-atm, whereas 24.1 μm-atm are measured at 60°N, showing a large increase of ozone with latitude at northern early spring (L_s = 13.3° for orbit 262). The other result of the fit, the surface albedo at 210 and 300 nm, shows a large increase of UV surface albedo from 41°N to 60°N, suggesting the presence of ice or frost on the ground. The deduced dust loading is low (0–0.2).

[32] As data spectra were averaged over a large number of individual spectra (250), the signal-to-noise ratio is very good (~3000) and the error bar σ_p associated with photon counting statistics (which dominates instrumental noise) is very low. The quality of the fit is measured by the

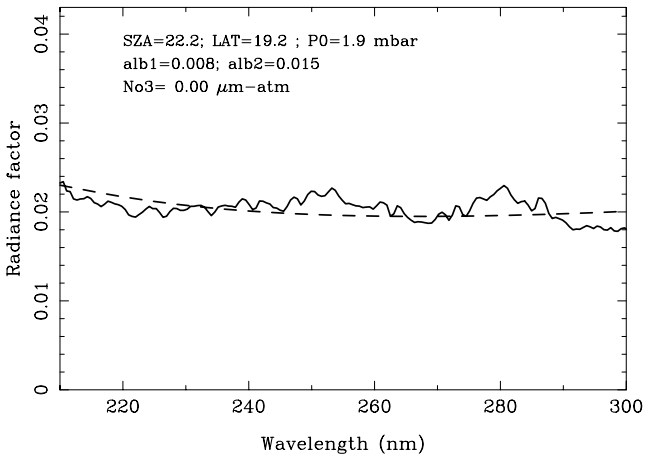

Figure 9. Radiance factor measured above Olympus Mons (solid line, orbit 1448) and radiance factor for the model reference spectrum (dashed line). Note that these spectra are almost constant with wavelength: the increase in surface albedo with wavelength and the decrease of Rayleigh scattering intensity tend to compensate.

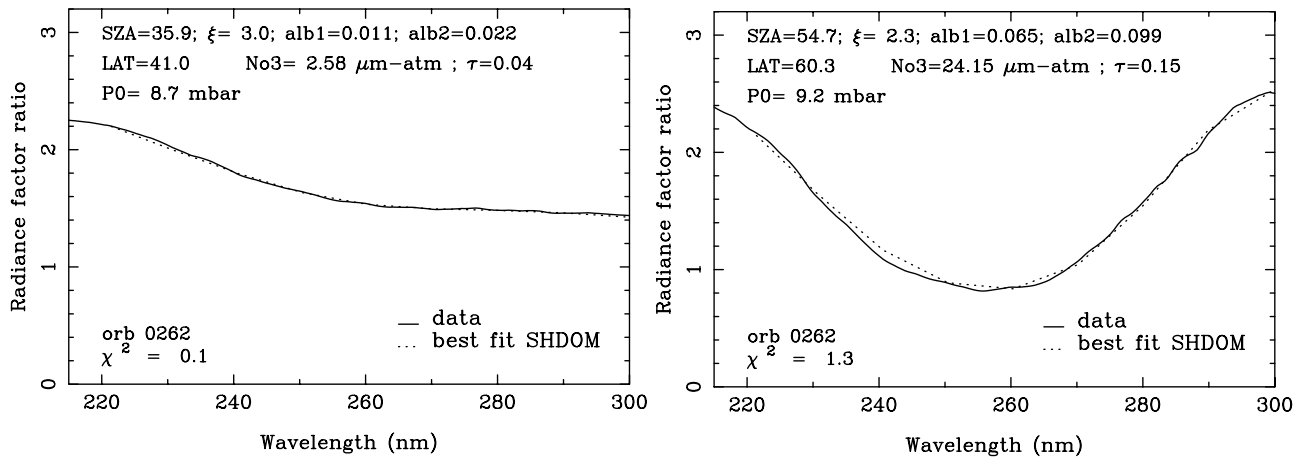

Figure 10. Two examples of fits for orbit 262, at two different latitudes: (left) 41°N and (right) 60°N. The data are the solid line, and the best fit is the dotted line. At 41°N, the retrieved ozone column density is 2.6 μm-atm, whereas at 60°N, the retrieved ozone column density is 24.1 μm-atm, showing a large increase of ozone with latitude at northern early spring (L_s = 13.3° for orbit 262). Other important parameters for radiative transfer computation are indicated, such as the solar zenith angle (SZA), the emission angle (ξ), and the surface pressure P_0. The values of the three other free parameters, surface albedo at 210 nm and 300 nm, dust opacity, and the χ^2 of the fit, are also indicated.

normalized χ^2 per point, which is computed by the Levenberg-Marquardt routine as:

$$\chi^2 = \frac{1}{N}\sum \frac{(\text{data} - \text{model})^2}{\sigma_p^2 + \sigma_m^2} \quad (2)$$

where N is the number of points on the spectrum (9) and σ_m is a modeling error linked to our assumptions, for instance small variations of the surface albedo from the assumed linear absorption. With a realistic σ_p and σ_m = 0, the resulting χ^2 is much larger than 1, while it should be of the order of 1, or more exactly of $(N - p)/N$ where p is the number of parameters to be fitted. Here, the value of $(N - p)/N$ is 0.6 (N = 9 and p = 4). To obtain a normalized χ^2 equal to 0.6 per point at the end of the χ^2 minimization process, we had to adjust the total sigma to a value of 0.03 on the relative spectrum. Thus the modeling error σ_m cannot be neglected.

3.5. Model Error σ_m

[33] The model error is linked to the modeling of the atmosphere (surface pressure, temperature, ozone vertical distribution, presence of dust or clouds), the main contribution being the uncertainties about the properties of dust, according to some testing of retrieval. To estimate the uncertainties and biases on the retrieved ozone column, we have tested our retrieval method on a set of spectra synthesized with the forward model. These spectra (for which the actual ozone column is known) were analyzed exactly as if they had been obtained with SPICAM. This study was made for three representative situations of our observations:

[34] 1. One case (a) with high surface pressure (9 mbar) and large SZA (70 degrees), leading to a high airmass factor, with an ozone column of 15 μm-atm. This situation corresponds to high northern latitudes, in which large ozone quantities are detected during the spring.

[35] 2. One case (b) with standard surface pressure (6 mbar) with the Sun at the zenith (SZA = 0) and 10 μm-atm of ozone. This case represents equatorial regions, and we check if high amounts of ozone can be misestimated.

[36] 3. A case (c) similar to the previous one with 1 μm-atm of ozone, to check whether ozone can be ''detected'' by our method in regions that are ozone-poor.

[37] In each case, we have studied the influence and possible biases induced by the following:

[38] 1. The presence of dust in the forward model (to model the influence of dust actually present in Mars atmosphere), the properties (ω, g) and vertical distribution of this dust.

[39] 2. The shape of vertical ozone profile predicted by GCM.

[40] 3. The radiance above Olympus Mons, which can be misestimated in our reference spectrum in the case of a poor absolute calibration.

[41] 4. The presence of clouds.

[42] In case (a), we have varied all parameters. The presence of dust leads to an underestimation of ozone column, with relative errors no larger than 10–20%, whatever the surface albedo (we tried surface albedo of 0.015 and 0.15 to bracket representative values, with dust parameters ω = 0.6, g = 0.88). It can lead to relative errors greater than 30% for dust opacities of 1, which only occurs during dust storms.

[43] Even in dust-rich atmospheres with a dust opacity of 0.6, uncertainties on ω (varied from 0.5 to .07) and g (varied from 0.8 to 0.9) rarely lead to errors larger than 20% on the retrieved ozone quantity, not more than the uncertainty on dust.

[44] The vertical profile of dust has been varied, following the formula proposed by *Conrath* [1975] for the dust vertical distribution, with γ (the so-called Conrath parameter) of 0.007 (representative of dust storms), 0.03 (standard case), and 0.05 (polar night). We also tested an homoge-

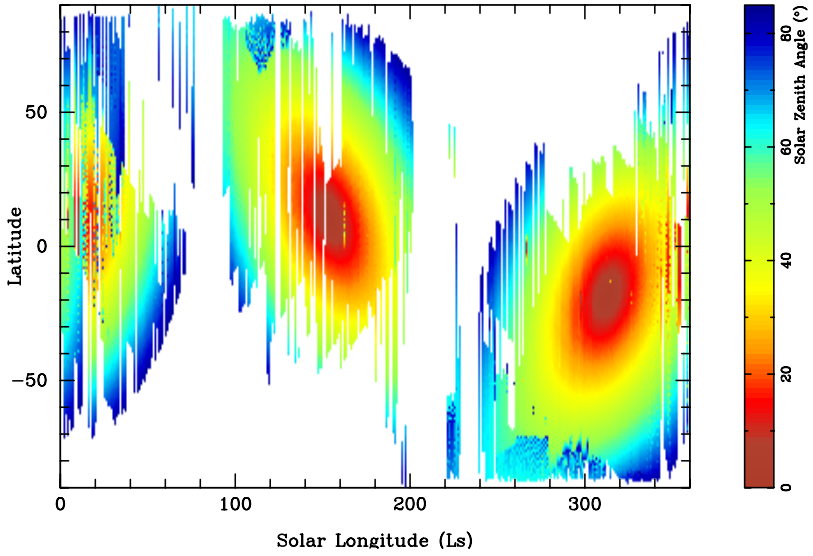

Figure 11. Coverage of SPICAM data in a latitude-season (solar longitude) plane. The color code represents the solar zenith angle (SZA) at the instant of observation. When several observations are realized in a one-degree L_s period of time, the averaged value of the SZA is represented. All spectra observed with SZA larger than 85° were rejected.

neous mixing of dust with the CO_2 distribution. The error associated with the presence of dust is not significantly increased by a change from the standard profile. In all cases, errors typically increase with solar zenith angle (higher air mass factor) and in presence of large aerosol loading. Errors tend to decrease in the case of high surface albedo. For case (c) (small ozone quantities), a strong dust opacity (typically 0.5) can induce an error of >1 μm-atm.

[45] We constrain the vertical profile of ozone using the prediction of the GCM for the same time and location (cases (a), (b) and (c)). To estimate the impact of this assumption on the retrieval, we ran two additional cases with the location changed by 10 degrees northward and southward (these profiles are rescaled to the same ozone column density). This is supposed to represent a fair uncertainty on the actual ozone vertical distribution, as the model suggests substantial profile variations within latitudinal bands 30 degrees wide (see Figure 4). Changes in the retrieved abundances of ozone do not exceed 10%, and thus errors associated with the ozone distribution is secondary compared to other sources of uncertainty.

[46] An error on the radiance above Olympus Mons would not affect the ozone quantity, since surface albedo is a free parameter. Any error on the reference radiance calibration will be compensated for by adjusting the retrieved surface albedo but not the ozone value.

[47] Finally, all these contributions lead to typical uncertainties on ozone column estimated to be around 10–15%, reaching 30% in some locations with important amounts of dust (opacity greater than 0.5). The presence of clouds can also lead to larger errors: a cloud opacity of 0.5, lofted between 20 and 30 km of altitude, leads to errors of 40 to 80% depending on the surface albedo. The error reaches nearly 100% for clouds opacity of 1 and low surface albedo. Yet, such high-opacity clouds only cover restricted areas. Thinner clouds (with opacities of 0.1–0.2), which are more frequent, lead to an average error of 15%.

4. Results

4.1. Ozone Column Global Climatology

[48] For each orbit, we computed the best fit of the observed spectrum with the forward model described above and the Levenberg-Marquardt fitting method, with four free parameters, ozone column density, surface albedo at 210 and 300 nm, and dust opacity.

[49] We then obtain, for each observed area of the Martian atmosphere, the integrated quantity of ozone present at the instant of the observation. In order to study the seasonal behavior, the longitude is here ignored, and the results are represented in the geographical latitude versus solar longitude (L_s) plane. The global coverage of SPICAM data is shown in Figure 11, where the color code represents the value of the solar zenith angle (SZA) at the time of observation. A noticeable point on this map is the distribution of available data. Few data are available at high latitudes. This is due both to illumination conditions, and to the need to share observing time with other instruments of Mars-Express: SPICAM is usually on at the same time as imagers, thus around the pericenter, while the high latitudes could only be observed far from pericenter. Moreover, there is a lack of data between $L_s = 70°$ and $L_s = 90°$, when the pericenter is on the night side, and between $L_s = 200°$ and $L_s = 240°$, during MARSIS radar antennas deployment. For these various reasons, the coverage in season and latitude is not complete.

[50] Figure 12 presents the ozone distribution from all the data analyzed so far, over more than one Martian year. This is the first Martian ozone column mapping ever obtained, showing in one scoop how SPICAM has led to fundamental progress in our understanding of Mars atmosphere. This

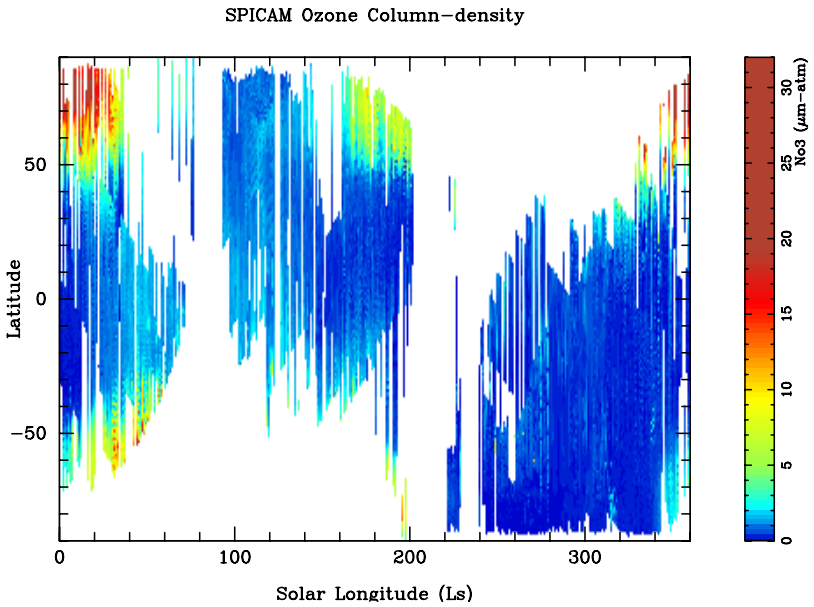

Figure 12. Ozone distribution (in μm-atm) as a function of latitude and solar longitude L_s, from $L_s = 0°$ to 360° (observations realized between 9 January 2004 and 21 November 2005). The data set coverage in season and latitude is variable, depending on observational and technical constraints. Sharp variations are measured in the ozone column density. The map is divided into one-degree solar longitude sectors. When several observations are realized in a one-degree L_s period of time, the averaged value of the ozone quantity is represented.

map is divided into sectors of one degree in solar longitude by one-degree in latitude. Each observation corresponds to a large range of Martian longitude. When several observations are realized in the same sector, we represent the averaged value of the ozone column (there are rarely more than 3 observations in the same sector). The period L_s = 331°–37° has been observed twice, in MY 27 and MY 28. The data displayed on the map at this period were averaged over the two years, but a separate study was made to look at the interannual variability (see further in this section).

[51] The striking feature of this map is the strong spatial and temporal variations in the ozone quantity, which makes Martian ozone behavior very different from ozone behavior on Earth. At equator and mid-latitudes, the ozone column density remains low throughout the year, and does not exceed 3 μm-atm. At high latitudes of both hemispheres, high ozone quantities (larger than 5 μm-atm) are observed at fall and early spring, and there is some evidence of such high values also in winter. These ozone concentrations disappear during the late spring, and are totally absent during the summer. This will be detailed in the following sections. For the northern hemisphere, maximum values are reaching 32 μm-atm at early spring ($L_s \sim 10°$), at latitudes 70–75°N. For the southern hemisphere, values around 12 μm-atm are measured at fall at latitudes 60–70°S. Unfortunately we do not have measurements at southern high latitudes between L_s = 60° and 180° (southern winter). Maximum values in the southern hemisphere are reached in local topographic depressions: up to 25 μm-atm are measured inside Hellas Basin (between 30°S and 55°S), at L_s = 40–60°. Some local increases on ozone column are also detected in Argyre Planitia (more details in section 5.2).

4.2. GCM Simulations of Ozone and Its Anticorrelation With Water Vapor

[52] In order to understand the main features of our ozone map, it is worthwhile to have in mind those of theoretical models. *Lefèvre et al.* [2004] presented the first three-dimensional model simulations of ozone on Mars. The overall behavior of the ozone seasonal evolution calculated by the model can be examined in Figure 13, showing the zonally averaged ozone column as a function of latitude and solar longitude. Note that values were averaged over 24 hours and are therefore a mean of daytime and nighttime abundances, not directly comparable with SPICAM measurements. Since there is more ozone during the night than during the day, it overestimates what SPICAM measures on the day side. The O_3 column evolution can be related to the water vapor abundance calculated by the model, also shown in Figure 13. *Montmessin et al.* [2004] largely discuss the results regarding the water cycle in the GCM. At first glance, the anticorrelation between ozone and water vapor column seems clearly visible. Ozone destruction is expected to be controlled by the abundance of the HO_x, and therefore by the species responsible for their presence, water vapor. This theoretical anticorrelation was first indirectly inferred from Mariner 9 results [*Lane et al.*, 1973]. At high latitudes of both hemispheres, the ozone column density is maximum in winter, when condensation on polar caps traps most of the atmospheric water vapor. Polar ozone is minimum in summer, indicating an efficient O_3 destruction by the HO_x radicals released from large amounts of water vapor and sunlight. It should be noted that the regions where the model

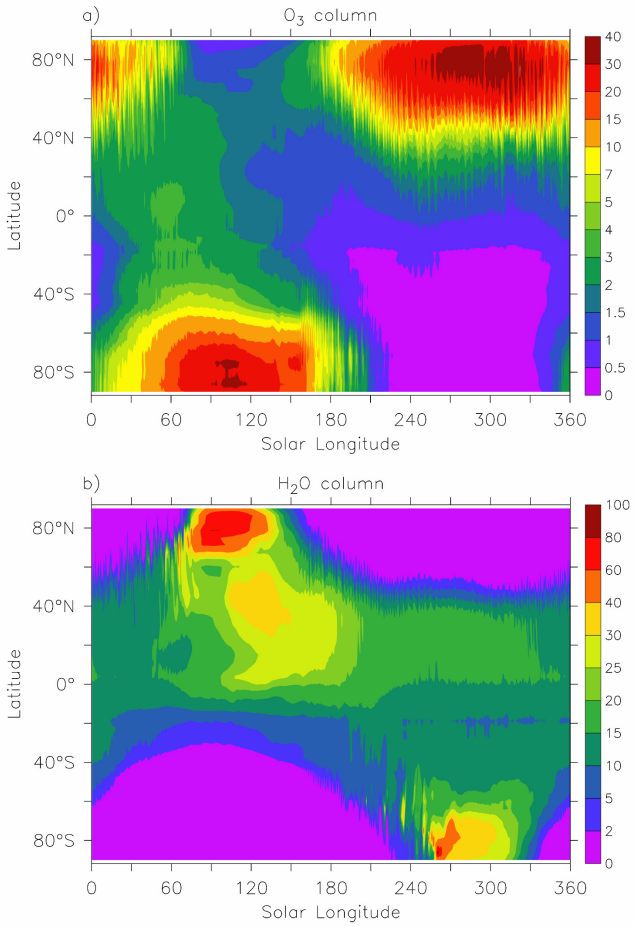

Figure 13. GCM map from *Lefèvre et al.* [2004]. (a) Zonally averaged ozone column density (μm-atm) and (b) zonally averaged water vapor column (precipitable microns, pr-μm), as a function of latitude and solar longitude. Values are averaged over 24 hours.

of Figure 13 predicts high levels of ozone are in winter high latitudes, where the lack of solar light prevents SPICAM nadir observations. Only the edges of these regions can be observed (Figure 12).

4.3. Seasonal Analysis

[53] The SPICAM ozone measurements and their comparison with other observations are now explored in more detail as a function of the season, characterized by the solar longitude L_s. In the following NH and SH are used for Northern and Southern hemisphere, respectively.

4.3.1. NH Spring/SH Fall (L_s = 0–90°)

[54] SPICAM measurements corresponding to the 0–90° L_s range were performed between 13 March 2004 (orbit number 202, L_s = 4°) and 20 August 2004 (orbit number 748, L_s = 77°). Figure 14 shows the ozone measurements for a few representative SPICAM observations performed during the NH early spring (SH early fall) and mid-spring. Results for late spring (60–90° L_s range) are shown in Figure 15.

[55] In the northern hemisphere, SPICAM observes very low O_3 column densities at low and mid latitudes (up to 40°N), typically not more than 2 μm-atm. On the contrary, very high ozone quantities are found at high latitudes in the early spring: values of 33 μm-atm are reached around 70°N, which are the highest values observed in the northern hemisphere over the whole Martian year. As a result, there is a strong latitudinal gradient in ozone concentration at latitudes around 40°N. In the southern hemisphere, the ozone latitudinal profile is qualitatively similar to that of the northern hemisphere, with low ozone quantities from 0 to 40°S, and higher quantities at higher latitudes. This concentration of ozone is however not as strong as in the northern hemisphere; the typical ozone column density is 10 μm-atm.

[56] Ozone at high northern latitudes shows a high variability from one orbit to the other: for a given latitude between 50° and 80°N, variations by a factor of three in the column density can be observed. The observations represented on Figure 14 do not sample the same local time and geographical longitude, which can cause some variability. The high variability above 50°N must have another origin, since the variability in the southern regions is smaller than in the northern hemisphere, whereas topographical variations are much larger in the southern hemisphere (old craterized terrains). Therefore the large variations in the northern regions are certainly not of topographical origin, but rather of dynamical origin. This behavior is predicted by the GCM. A striking feature in the GCM ozone map (Figure 13) is the considerable day-to-day variability associated with the dynamical disturbances of the northern polar vortex (as the GCM map has been zonally averaged, the only source of variability is due to meteorological effects). Baroclinic waves have a maximum activity in late winter and spring. This results in rapid evolving distortions of the polar vortex edge that are easily identifiable by the steep O_3 gradients. *Barth* [1985] attributed the large O_3 variability to rapid variations of the H_2O content, but *Lefèvre et al.* [2004] explained that O_3 can be considered as a quasi-passive tracer inside the polar vortex at least until spring equinox. Its variations over short timescales at latitudes close to the vortex edge may be entirely attributed to variations in the shape of the polar vortex. These predicted day-to-day variations are observed by SPICAM.

[57] *Barth et al.* [1973] reported from Mariner 9 data that the maximal amount of ozone during spring is found at high northern latitude. Their values (5 to 17 μm-atm at L_s = 45°) are compatible with SPICAM measurements, and also show a large variability in the northern hemisphere.

[58] *Clancy et al.* [1999] employed the Faint Object Spectrograph (FOS) on the HST to measure the latitudinal distribution of ozone at L_s = 10° (September 1996) and L_s = 61° (January 1997). Observations at L_s = 10°, shortly after the northern spring equinox, are compared to our data in Figure 14, showing an excellent agreement for low to mid latitudes. Above 40°N, Clancy data are inside the variability range of SPICAM data. Later in the NH spring season, SPICAM observes values generally lower than previous measurements from *Clancy et al.* [1999], at L_s = 61°, and *Fast et al.* [2006], at L_s = 74° (in March 1995, using infrared spectroscopy), as shown in right panel of Figure 15), especially for low to mid latitudes. This could be explained by a variability from one year to the other in

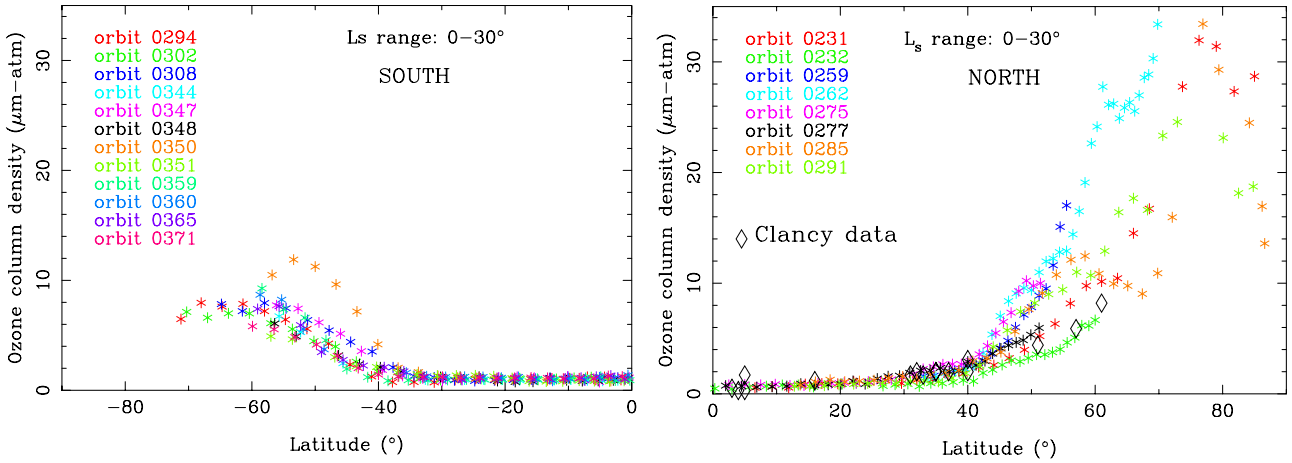

Figure 14. Ozone measurements (in μm-atm) for a few representative observations in the 0–30° L_s range: (left) for the southern hemisphere (early fall) and (right) for the northern hemisphere (early spring). Black diamonds represent data from *Clancy et al.* [1999] (at L_s = 10°), in good agreement with our measurements.

the decrease of the water vapor saturation level, called hygropause (see more details in section 5).

4.3.2. NH Summer/SH Winter (L_s = 90–180°)

[59] SPICAM measurements corresponding to the 90–180° L_s range were performed between 28 September 2004 (orbit number 887, L_s = 93°) and 22 March 2005 (orbit number 1513, L_s = 180°). Results are shown in Figure 16.

[60] Ozone quantities are still low at moderate latitude, with values below 3 μm-atm between latitudes 30°S and 40°N. At high southern latitudes, there are few observations, but the gradient in ozone quantity around 40°S observed during SH fall seems to be still present with a similar amplitude. At high northern latitudes, the ozone column that was observed to decrease during the NH spring gets below 2 μm-atm in the early NH summer (90–120° L_s range). It slightly reappears during the mid-summer (120–150° L_s range), and values up to 10 μm-atm at 60–70°N are observed at the end of summer (with a high variability).

[61] There were few published data of ozone in NH summer: Mariner 9 found ozone to be below the detection limit of the instrument (3 μm-atm) above the North polar cap at L_s = 120°, which is consistent with SPICAM data. Since then, only two measurements had been performed by *Fast et al.* [2006] at L_s = 102° (in July 1993) and 115° (in March 1999), finding less than 4 μm-atm in the NH. SPICAM has thus largely increased the seasonal and geographical coverage available.

4.3.3. NH Fall/SH Spring (L_s = 180–270°)

[62] SPICAM measurements corresponding to the 180–270° L_s range were performed between 23 March 2005 (orbit number 1515, L_s = 180°) and 16 August 2005 (orbit number 2037, L_s = 270°). Retrieved ozone column densities are shown on Figure 17.

[63] There are nearly no SPICAM observation of northern hemisphere between L_s = 210° and 270°, but at the beginning of the NH fall the large amounts of ozone at high northern latitudes are still observed, even if somewhat smaller than at the end of the NH summer. In the southern hemisphere, the high ozone quantities observed around

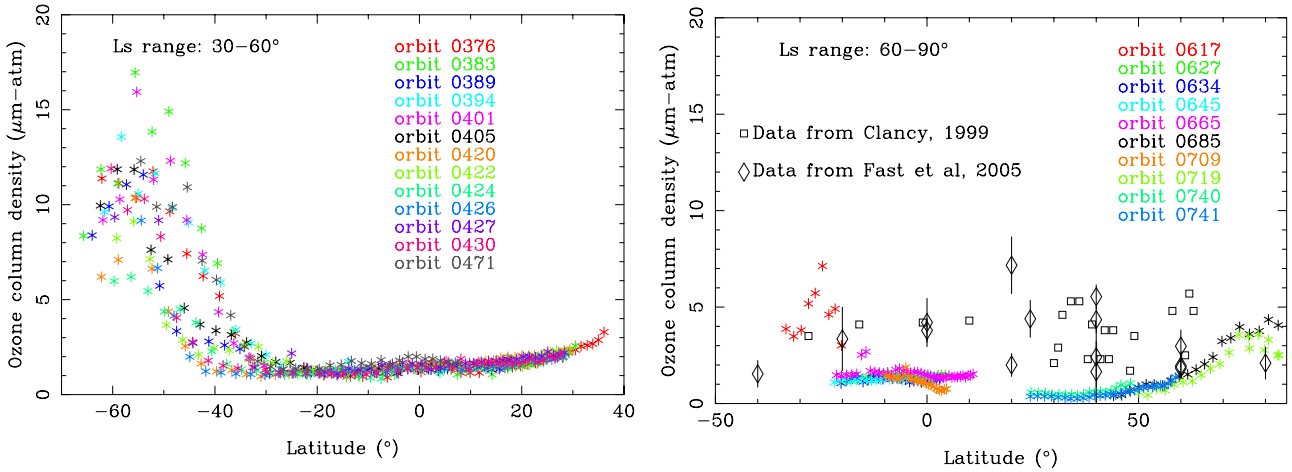

Figure 15. Ozone measurements for a few representative observations (left) in the 30–60° L_s range and (right) in the 60–90° L_s range. Data from the Earth (Infrared heterodyne spectroscopy [*Fast et al.*, 2006]), at L_s = 74° (diamonds), and data from *Clancy et al.* [1999] (for L_s = 61°, squares) are also shown.

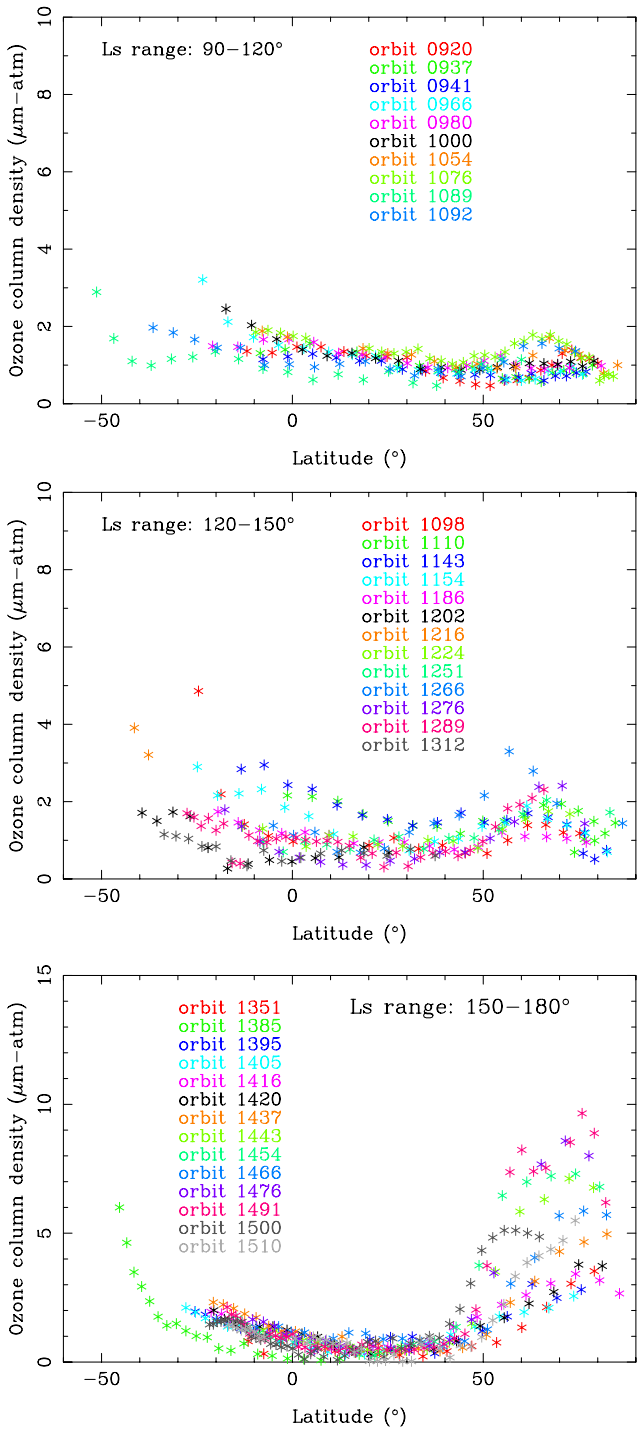

Figure 16. Ozone measurements for a few representative observations (top) in the 90–120° L_s range, (middle) in the 120–150° L_s range, and (bottom) in the 150–180° L_s range.

70°S, that were present since the SH fall, rapidly disappear around $L_s = 210°$ (see Figure 17, top and middle). A similar phenomenon has been observed in the northern hemisphere at the end of the NH spring (see section 4.3.1). This is the result of the release of water vapor from the receding south polar cap (Figure 13).

[64] The low ozone quantities found between 50°S and 20°N, that never exceed 2 μm-atm, are consistent with the measurements made by *Fast et al.* [2006]. They measured O_3 from 60°S to 40°N at $L_s = 202°$ (in June 2003) and from 80°S to 20°N at $L_s = 208°$ (in June 1998). Of these

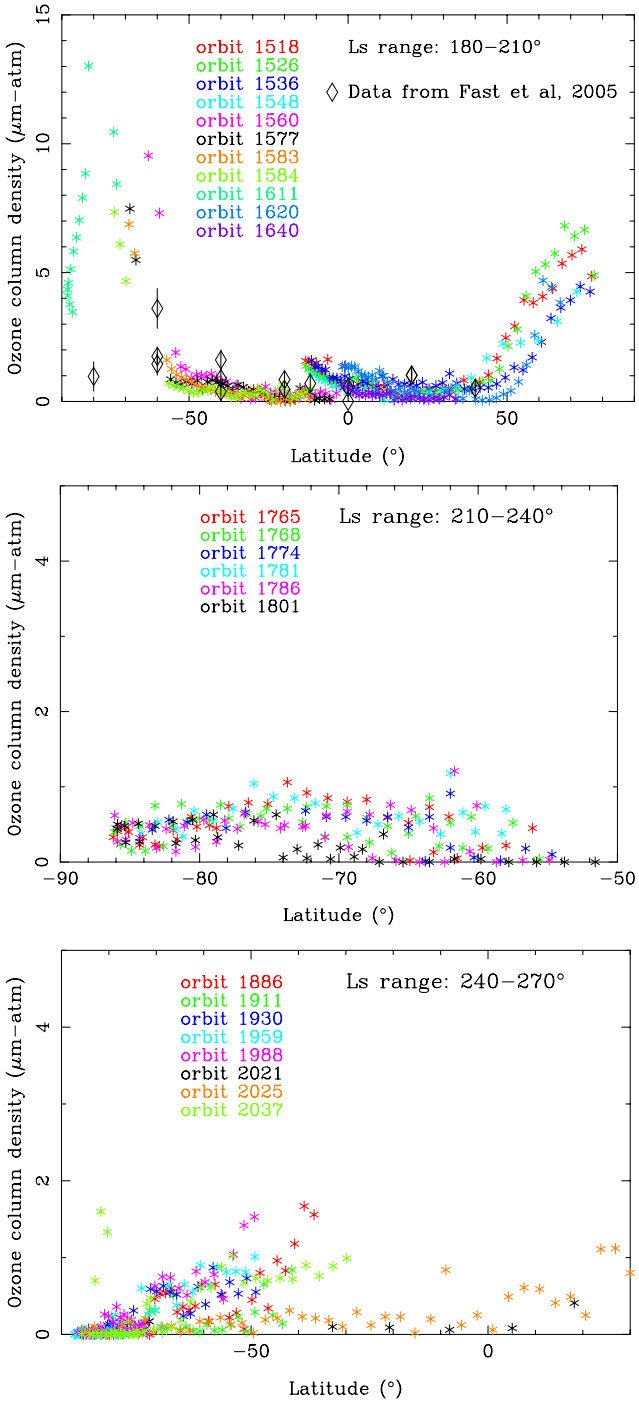

Figure 17. Ozone measurements for a few representative observations (top) in the 180–210° L_s range (including data from *Fast et al.* [2006] at $L_s = 202°$, March 2003, $L_s = 208°$, June 1988), (middle) in the 210–240° L_s range, and (bottom) in the 240–270° L_s range.

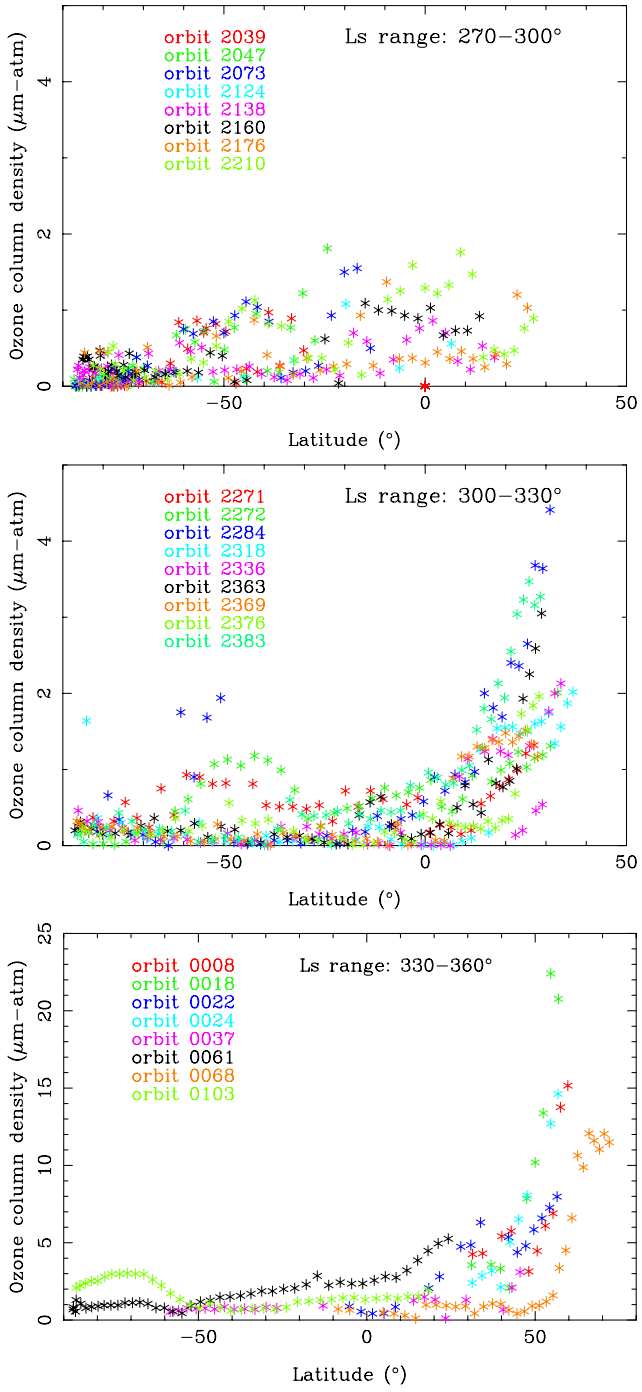

Figure 18. Ozone retrieval during MY 27 as a function of latitude for a few representative orbits (top) in the 270–300° L_s range, (middle) in the 300–330° L_s range, and (bottom) in the 330–360° L_s range.

measurements, 13 points out of 14 are below 2 μm-atm, in good agreement with SPICAM results.

4.3.4. NH Winter/SH Summer (L_s = 270–360)

[65] SPICAM measurements corresponding to the 270–360° L_s range were performed between 16 August 2005 (orbit number 2039, L_s = 270°) and 21 November 2005 (orbit number 2384, L_s = 328°), and between 9 January 2004 (orbit number 8, L_s = 331°) and 5 March 2004 (orbit number 174, L_s = 360°).

[66] Figure 18 shows ozone measurements for a few representative orbits. For the 270–330° L_s range, quantities are usually lower than 2 μm-atm in SH and low latitudes of NH. High ozone amounts are measured at high northern latitudes in the period L_s = 330–360° (bottom panel). The data show a great variability: the ozone column densities can vary by a factor of 4 in the latitude range 50°–70°N. This can be related to the high variability predicted by the GCM at polar latitudes at this season and explained by the day-to-day variations of the shape of the polar vortex (see also section 4.3.1).

[67] For the 300–330° L_s range, the covered latitude range is 90°S–40°N. Retrieved quantities remain usually lower than 1 μm-atm in the northern hemisphere, except for some orbits where an increase is detected, reaching 4 μm-atm at 30°N, likely indicating high ozone amounts at higher north latitudes that could not be directly observed.

[68] The wintertime (L_s = 330°–360°) measurements by Mariner 9 revealed the largest O_3 amounts ever observed on Mars. Values up to 60 μm-atm were detected in the 50°–

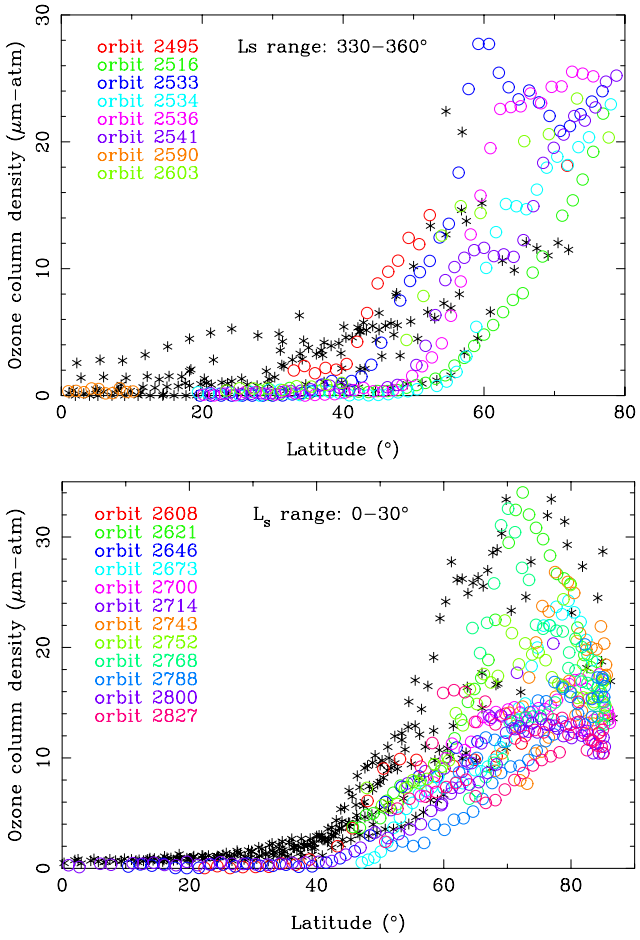

Figure 19. Black stars, data from MY 27 also represented in Figures 18 and 14. Color circles, data from MY 28. (top) Ozone column for northern latitudes in the 330–360° L_s range. (bottom) Ozone column for northern latitudes in the 0–30° L_s range.

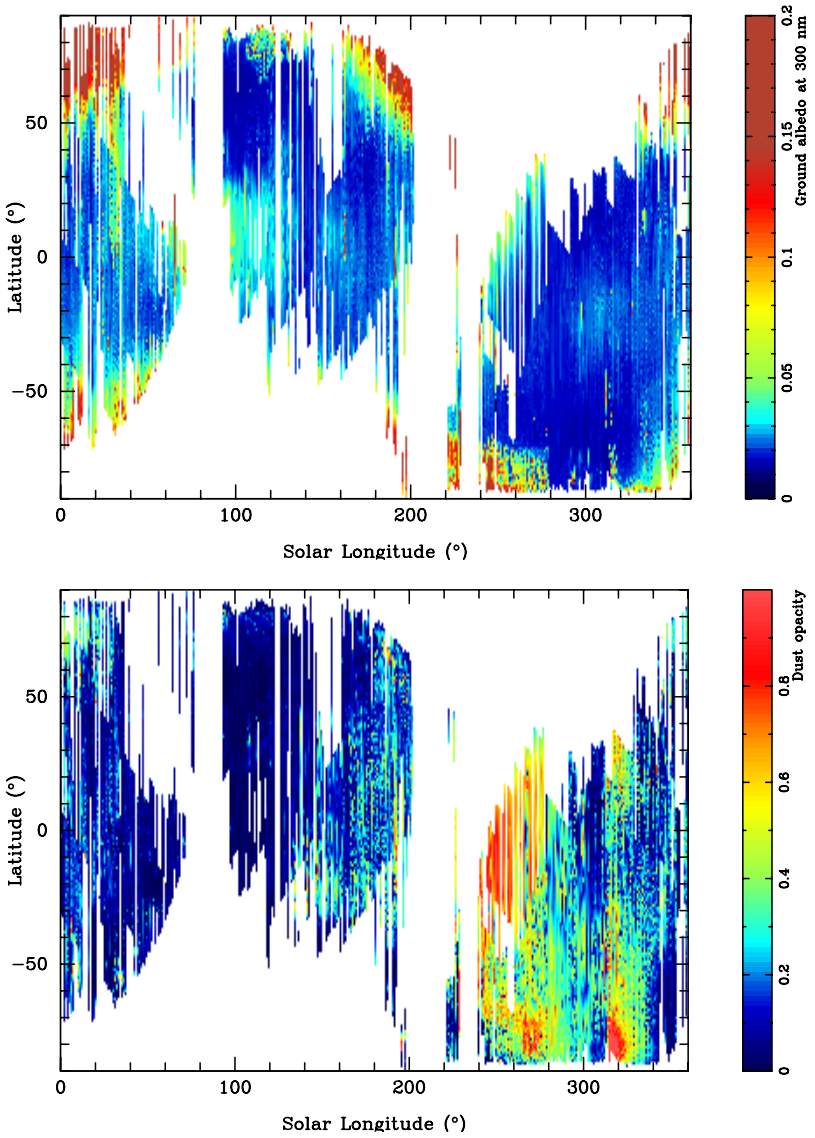

Figure 20. (top) Latitude-Ls map of surface albedo at 300 nm, as outputs of fits. The Martian ground is usually very dark in the UV, except over the polar caps. A large increase in the albedo in the equatorial regions between $L_s = 50°$ and $L_s = 130°$ has to be linked to the equatorial cloud belt at this time of the year. (bottom) Latitude-Ls map of dust, as outputs of fits.

75°N latitude band [*Wherbein et al.*, 1979], and showed also wide day-to-day variations. From the Mariner 9 individual observations presented by *Traub et al.* [1979], it appears that the O_3 amounts at high northern latitudes may fall anywhere in the range 5–40 μm-atm from one orbit to the other, which is not in contradiction with SPICAM results.

4.3.5. Interannual Variability

[69] The L_s range 330°–30° was observed by Mars Express consecutively during MY 27 and MY 28. Figure 19 shows the comparison of the retrieved ozone columns for these two years. The large ozone variability during northern late-winter early-spring is confirmed and no interannual variability can be deduced from SPICAM measurements alone, as differences between MY27 and MY28 fall within the amplitude of variations between orbits. However, the study of ozone is promising to reveal potential variability as this species is extremely reactive and therefore extremely sensitive to even slight meteorologic changes (water vapor, temperature and dust loading).

4.3.6. Surface Albedo and Dust Maps

[70] The three other free parameters of the model (beyond the ozone quantity), the surface albedo at 210 nm, the surface albedo at 300 nm and dust opacity, are also very interesting outputs of the fits.

[71] The wavelength dependence of the Martian surface albedo is poorly known over the 210 to 300 nm region. The Martian ground is usually very dark in the UV, except over the polar caps. *Clancy et al.* [1999] adopted a wavelength independent value of 0.015 for the Martian surface albedo, from HST UV observations. The surface albedo map retrieved with SPICAM at 300 nm is shown in Figure 20 (top) as a function of latitude and season. The longitude has been zonally averaged. Albedo values are in the range 0.015–0.2. A representative range of values of the dark Martian ground is 0.015–0.03 for $\lambda = 300$ nm. We find that ground albedo

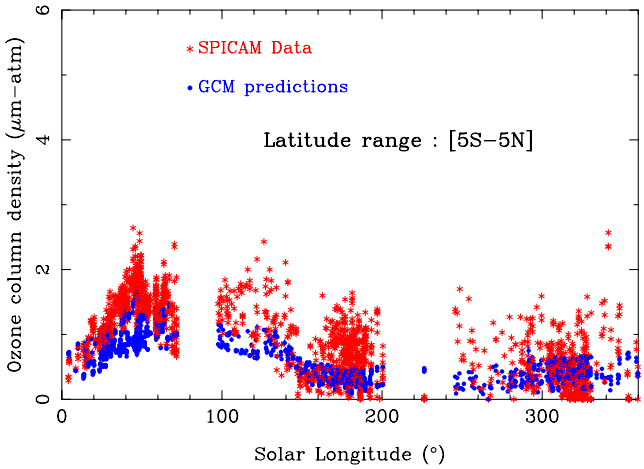

Figure 21. Comparison between retrieved ozone column densities and GCM predictions at the equator (LAT = 5°S–5°N). Note the global agreement between data and model.

at 210 nm is a little smaller (between 0.01 and 0.015) than at 300 nm. The latitudinal and seasonal variations of albedo at 210 nm are very similar to those detailed at 300 nm.

[72] The icy ground of polar caps is much brighter than the soil (up to 10 times brighter). Progressive disappearance of the south polar cap during southern spring (from L_s = 180° to L_s = 270°) clearly appears. The disappearance of north polar cap between L_s = 10° and L_s = 90°, during northern spring, is also observed. The albedo increase in equatorial regions between L_s = 50° and L_s = 130° is most likely linked to the well-known equatorial cloud belt first identified by *Clancy et al.* [1996b] around Mars aphelion. Their presence is directly related to the low altitude of water vapor saturation at aphelion [*Clancy et al.*, 1996a]. Clouds are also present at higher latitudes, around 50–60°N at this end of northern summer (L_s = 170–200°).

[73] Figure 20 (bottom) represents the retrieved dust opacity (scaled to 6.1 mbar). The seasonal variation of dust opacity as deduced from SPICAM data in UV agrees very well with the common picture of the Martian dust cycle: very clear conditions ($\tau \sim 0.1$) are observed around northern summer solstice (L_s 90°) while dramatically greater abundances ($\tau > 1$) are obtained during southern spring and summer (L_s 200 to 330°). The dusty conditions of perihelion are a salient feature of Mars climate, with winds producing stronger lifting at that season compared to aphelion. A more detailed analysis will help us determine where source regions are located and the comparison with other instruments of Mars Express will yield dust optical behavior from UV to far infrared, thereby giving constraints on dust microphysical properties (e.g., mean radius). The overall agreement of our dust seasonal map with previous monitoring of dust activity on Mars (especially in the infrared, see Smith et al., 2004) supports the consistency of our retrieval method. However, some biases and uncertainties remain. First, retrieved opacity depends on the choice of both γ and g for dust, which have been held fixed for the sake of simplicity. While it should be possible in the future to deduce the real scattering properties of dust in UV, this is not the scope of the present study which focuses instead on ozone retrieval. Second, surface albedo and atmospheric dust loading can be considered independent parameters in a first approach. However, there are cases where the inversion algorithm increases both simultaneously as their effect neutralizes each other (radiance increases with albedo and/or with a decrease of the dust loading). In most cases however, dust is well differentiated from surface albedo.

5. Discussion and Comparison to GCM Predictions

[74] Some of the nadir SPICAM UV results are now compared to the three-dimensional distribution of ozone computed by the General Circulation Model (GCM) described by *Lefèvre et al.* [2004]. Note that O_3 total column GCM predictions were extracted from the GCM at the same location, local time and, of course, solar longitude, when the measurements were performed.

5.1. Global GCM Comparisons

[75] Figure 21 represents the ozone behavior around the equator (in a range 5°S–5°N), in the data and in the model. SPICAM measurements at the equator never exceed 3 μm-atm all year, and most of the time they are even smaller than 2 μm-atm. They show a globally

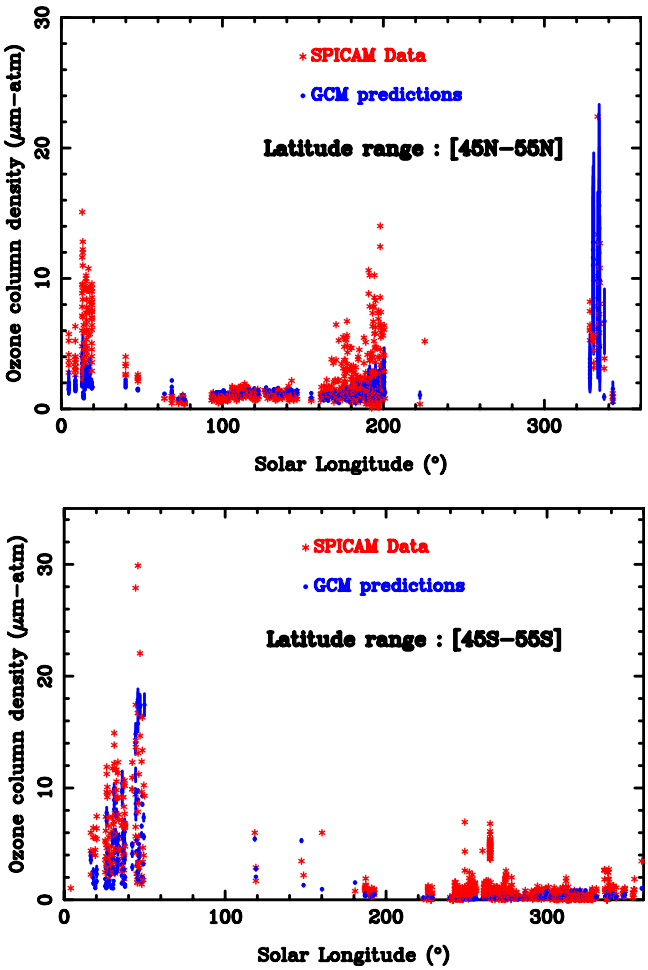

Figure 22. Comparison between retrieved ozone column densities and GCM predictions at (top) northern latitudes (LAT = 45–55°N) and (bottom) southern latitudes (LAT = 45–55°S.)

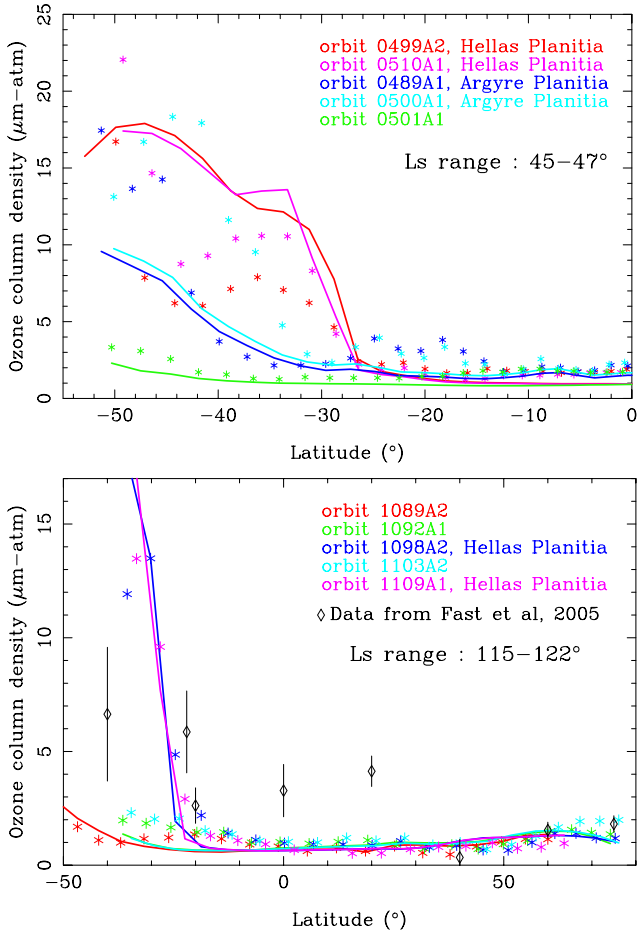

Figure 23. Comparison between data and GCM for the (top) 45−47° L_s range and (bottom) 115−112° L_s range. The various GCM curves (solid lines) are taken at longitudes with different surface elevation: −6000 m for Hellas Planitia (red and purple curves), −2000 m for Argyre Planitia (blue curves), and +1000 m elsewhere (green curve). The highly variable topography in the southern hemisphere explains much of the variability of the GCM computations. Orbits showing largest GCM ozone quantities correspond to the flyby of Hellas Planitia. This local O_3 enhancement predicted by the model is confirmed by SPICAM data, but to a lesser degree. The local enhancement on Argyre is equally present in both data and model. Ozone data from IR spectroscopy (March 1995 [*Fast et al.*, 2006]) are also represented.

good agreement with the GCM model at the equator over all the seasons, and the small increase around aphelion (L_s = 60°−120°) is seen both in data and model, even if GCM values are slightly lower than SPICAM measurements. *Clancy and Nair* [1996] explained that around aphelion, the cold and dust-free atmosphere leads to a low saturation altitude for water vapor (10−15 km). This process is argued to create an enhancement of Martian low to mid latitudes ozone above ≃20 km altitude, referred by these authors as to the "aphelion ozone layer" and which raises the observed total column at this period.

[76] Total ozone at northern high latitudes (45°N−55°N range) is represented on the right of Figure 22. The GCM fails to reproduce the important amounts of ozone measured by SPICAM (5−15 μm-atm) at L_s = 0−40° (early spring) and 170−200° (early fall). However, data during late winter are in good agreement with GCM, and one important feature is the high variability of ozone quantities, present both in the data and in the model. Total ozone at southern high latitudes (45°S−55°S range) is represented on the left of Figure 22, showing a better agreement even if ozone quantities are also slightly underestimated by GCM.

5.2. Case of Hellas and Argyre Planitias

[77] In the southern hemisphere, the variable topography of the craterized southern highlands leads to important effects. During southern fall and winter, large amounts of ozone are detected inside Hellas Planitia, with a maximum of 23 μm-atm, measured at L_s = 46° (Figure 23, left). *Fast*

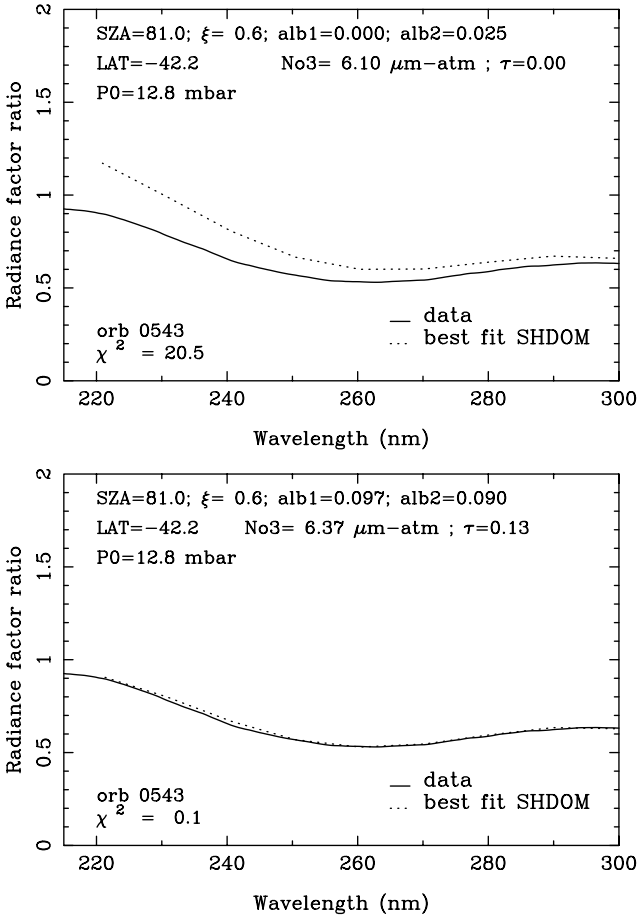

Figure 24. Examples of fit of orbit 543 (on 23 June 2004, L_s = 51.2°) when passing above Hellas Planitia. (top) Fit without dust. The signal is very low, and even with putting a surface albedo as low as possible, it is impossible to reproduce such a low intensity with the model because of the contribution of Rayleigh scattering. There must be something else which absorbs solar photons: dust. (bottom) Fit with dust. The fit is excellent. Dust has been included with ω = 0.6 and g = 0.88. The best fit gives a dust opacity of 0.13 at 6.1 mbar, which corresponds to a real opacity of 0.27 inside Hellas. Surface albedo is high, revealing some ice inside the depression. The retrieved ozone quantity is 5% greater than without dust.

et al. [2006] measure ozone values up to 7 μm-atm in the SH, between LAT = −20 and −40°, at L_s = 115°. These authors indicate that the 40°S IR measurements were on the southern limb of the observable disk of Mars as seen from Earth and may contain contribution from higher latitudes due to the wider coverage of the beam at that position, amplifying any tracking errors. The highest of the two retrievals at 20°S from *Fast et al.* [2006] in Figure 23 (right) is located north of Hellas: that spectrum could have a contribution from Hellas. The other retrieval at 20°S shows a much lower abundance, related to its midpoint longitude well away from Hellas.

[78] The various curves in Figure 23 correspond to the GCM predictions associated with these orbits with different longitudes. Ozone variability in the GCM computations is directly linked to the drastic changes in topography between the different orbits. Orbits showing high GCM ozone quantities correspond to the flyby of Hellas Planitia, where the pressure strongly increases (up to a surface pressure of 12.8 mbar for an elevation of −6800 m), increasing the ozone column up to 18 μm-atm in the model (orbit numbers 499 and 510 in Figure 23). This unique model prediction is confirmed by the data: during southern fall and winter, there is indeed more ozone in Hellas Planitia than anywhere else.

[79] Inside Hellas Planitia, dust is absolutely needed to fit the data, as shown in Figure 24. This figure shows two examples of fits, one without dust and one with dust. The intensity over Hellas is so low that it is impossible to reproduce it with a model without dust, but when including dust the fit becomes excellent. The coupling between surface albedo and dust is large, but the mean value of dust optical thickness found inside Hellas Planitia is 0.4 (at a surface pressure of 12.8 mbar), and the surface albedo is around 0.1, which is very high. It is wintertime in the southern hemisphere, so it is possible that Hellas Planitia is covered with ice at this period of time.

[80] SPICAM data also show an increase in the ozone column density when flying above Argyre Planitia (around 15–18 μm-atm inside Argyre Planitia, against 2–4 μm-atm outside (see orbits 489 and 500 in Figure 23 (left), compared to orbit 501), but not as important as for Hellas Planitia.

6. Conclusion

[81] This work describes the analysis of nadir SPICAM/Mars Express UV data. The resulting data set is the most complete ever obtained of the dayside ozone distribution in the Martian atmosphere.

[82] Comparison with Global Circulation Model [*Lefèvre et al.*, 2004] shows that GCM predictions are in generally good agreement with the overall ozone behavior that is described in this paper. Features such as the high variability in northern high latitudes during late winter-early spring, the increase of ozone at the equator around aphelion period or the local increase of ozone inside Hellas and Argyre, are indeed predicted by the GCM.

[83] However, SPICAM values are larger than the GCM predictions at high latitudes of both hemispheres, when important amounts of ozone are found (during early spring for the northern hemisphere and fall during southern hemisphere). GCM also underestimates ozone at low to mid latitudes during the aphelion period, in agreement with the conclusions of *Fast et al.* [2006].

[84] This new data set will improve significantly our knowledge of the ozone spatiotemporal distribution on Mars, providing the strongest observational constraints to date. This will help make further progress toward a quantitative understanding of the Martian photochemistry, allowing in turn through modeling the estimation of some chemicals difficult or impossible to measure, and important for "survival" of organic material at the surface (HO_x for example).

[85] Our understanding of the overall ozone climatology will also be improved by combining different SPICAM data sets: Ozone vertical distribution has been studied with the same instrument through stellar occultations [see *Lebonnois et al.*, 2006], as well as temperature and dust opacity profiles [*Montmessin et al.*, 2006]. Solar occultations should allow simultaneous retrieval of both ozone and water vapor profiles, and $O_2(^1\Delta_g)$ emissions at 1.27 μm give access to the dayside amount of ozone above 20 km altitude [*Fedorova et al.*, 2006b]. Indeed, SPICAM UV/IR is the first instrument able to measure simultaneously the vertical column density of ozone in the UV and O_2 emission in the IR, which is an indirect way to probe ozone above 20 km. SPICAM is also able to measure, simultaneously with ozone, the column density of water vapor in the near IR at 1.38 μm [*Fedorova et al.*, 2006a], yielding the first global experimental correlation between H_2O and ozone distributions. A global scale H_2O vs O_3 correlation study is work in progress.

[86] **Acknowledgments.** Mars Express is a space mission from ESA (European Space Agency). We wish to express our gratitude to all ESA members who participated in this successful mission. We thank also Astrium Corp. for the design and construction of the spacecraft. We thank our collaborators at the three institutes for the design and fabrication of the instrument (Service d'Aéronomie/France, BIRA/Belgium, and IKI/Moscow) and in particular the SPICAM project manager Emmanuel Dimarellis and the engineer Aurélie Rébérac at Service d'Aéronomie. We wish to thank CNRS and CNES for financing SPICAM in France. We wish to thank the Space Division of the Belgian Federal Science Policy Office for supporting this project through the ESA PRODEX program. The Russian team acknowledges support of RFFI grant 04-02-16856-a.

References

Barth, C. A. (1985), The photochemistry of the atmosphere of Mars, in *The Photochemistry of Atmospheres: Earth, the Other Planets, and Comets*, edited by J. S. Levine, pp. 337–392, Elsevier, New York.

Barth, C. A., and C. W. Hord (1971), Mariner ultraviolet spectrometer: Topography and polar cap, *Science*, *173*(3993), 197–201.

Barth, C. A., C. W. Hord, A. I. Stewart, A. L. Lane, M. L. Duck, and G. P. Anderson (1973), Mariner 9 ultraviolet spectrometer experiment: Seasonal variation of ozone on Mars, *Science*, *179*, 795–796.

Bertaux, J.-L., et al. (2000), The study of the Martian atmosphere from top to bottom with SPICAM light on Mars Express, *Planet. Space Sci.*, *48*(12–14), 1303–1320.

Bertaux, J.-L., et al. (2006), SPICAM on board Mars Express: Instrument, operations, observing modes, and overview of typical results, *J. Geophys. Res.*, doi:10.1029/2006JE002690, in press.

Bhartia, P. K., and C. Wellemeyer (2002), TOMS-V8 total O_3 algorithm, in *OMI Algorithm Theoretical Basis Document*, vol. 2, edited by P. K. Bhartia, pp. 15–32, NASA Goddard Space Flight Cent., Greenbelt, Md.

Bhartia, P. K., R. D. McPeters, C. L. Mateer, L. E. Flynn, and C. Wellemeyer (1996), Algorithm for the estimation of vertical ozone profiles from the backscattered ultraviolet technique, *J. Geophys. Res.*, *101*, 18,793–18,806.

Blamont, J. E., and E. Chassefière (1993), First detection of ozone in the middle atmosphere of Mars from solar occultation measurements, *Icarus*, *104*, 324–336.

Clancy, R. T., and H. Nair (1996), Annual (perihelion-aphelion) cycles in the photochemical behavior of the global Mars atmosphere, *J. Geophys. Res.*, *101*(E5), 12,785–12,790.

Clancy, R. T., M. J. Wolff, P. B. James, E. Smith, Y. N. Billawala, S. W. Lee, and M. Callan (1996a), Mars ozone measurements near the 1995 aphelion: Hubble Space Telescope ultraviolet spectroscopy with the Faint Object Spectrograph, *J. Geophys. Res.*, *101*(E5), 12,777–12,783.

Clancy, R. T., A. W. Grossman, M. J. Wolff, P. B. James, Y. N. Billawala, B. J. Sandor, S. W. Lee, and D. J. Rudy (1996b), Water vapor saturation at low altitudes around Mars aphelion: A key to Mars climate?, *Icarus*, *122*, 36–62.

Clancy, R. T., M. J. Wolff, and P. B. James (1999), Minimal aerosol loading and global increases in atmospheric ozone during the 1996–1997 Martian northern spring season, *Icarus*, *138*, 49–63.

Clancy, R. T., B. J. Sandor, M. J. Wolff, P. R. Christensen, M. D. Smith, J. C. Pearl, B. J. Conrath, and R. J. Wilson (2000), An intercomparison of ground-based millimeter, MGS TES, and Viking atmospheric temperature measurements: Seasonal and interannual variability of temperatures and dust loading in the global Mars atmosphere, *J. Geophys. Res.*, *105*, 9553–9572.

Conrath, B. J. (1975), Thermal structure of the Martian atmosphere during the dissipation of the dust storm of 1971, *Icarus*, *24*, 36–46.

Dave, J. V., and C. L. Mateer (1967), A preliminary study on the possibility of estimating total atmospheric ozone from satellite Measurements, *J. Atmos. Sci.*, *24*, 414–427.

Espenak, F., M. J. Mumma, T. Kostiuk, and D. Zipoy (1991), Ground-based infrared measurements of the global distribution of ozone in the atmosphere of Mars, *Icarus*, *92*, 252–262.

Evans, K. F. (1998), The spherical harmonics discrete ordinate method for three-dimentional atmospheric radiative transfer, *J. Atmos. Sci.*, *55*, 429–446.

Fast, K., et al. (2006), Ozone abundance on Mars from infrared heterodyne spectra, *Icarus*, *181*, 419–431.

Fedorova, A., O. Korablev, J.-L. Bertaux, A. Rodin, A. Kiselev, and S. Perrier (2006a), Mars water vapor abundance from SPICAM IR spectrometer: Seasonal and geographic distributions, *J. Geophys. Res.*, *111*, E09S08, doi:10.1029/2006JE002695.

Fedorova, A., O. Korablev, S. Perrier, J.-L. Bertaux, F. Lefèvre, and A. Rodin (2006b), Observation of O2 1.27 μm dayglow by SPICAM IR: Seasonal distribution for first Martian year of Mars Express, *J. Geophys. Res.*, *111*, E09S07, doi:10.1029/2006JE002694.

Forget, F., F. Hourdin, R. Fournier, C. Hourdin, O. Talagrand, M. Collins, S. R. Lewis, P. L. Read, and J.-P. Huot (1999), Improved general circulation models of the Martian atmosphere from the surface to above 80 km, *J. Geophys. Res.*, *104*(E10), 24,155–24,176.

James, P. B., R. T. Clancy, S. W. Lee, L. J. Martin, R. B. Singer, E. Smith, R. A. Kahn, and R. W. Zurek (1994), Monitoring Mars with the Hubble Space Telescope: 1990–1991 observations, *Icarus*, *109*, 79–101.

Krasnopolsky, V. A. (2003), Mapping of Mars O_2 1.27 μm dayglow at four seasonal points, *Icarus*, *165*, 315–325.

Krasnopolsky, V. A., and V. A. Parshev (1979), Ozone photochemistry of the Martian lower atmosphere, *Planet. Space Sci.*, *27*, 113–120.

Lane, A. L., C. A. Barth, C. W. Hord, and A. I. Stewart (1973), Mariner 9 ultraviolet spectrometer experiment: Observations of ozone on Mars, *Icarus*, *18*, 102–108.

Lebonnois, S., E. Quémerais, F. Montmessin, F. Lefèvre, S. Perrier, J.-L. Bertaux, and F. Forget (2006), Vertical distribution of ozone on Mars as measured by SPICAM/Mars Express using stellar occultations, *J. Geophys. Res.*, *111*, E09S05, doi:10.1029/2005JE002643.

Lefèvre, F., S. Lebonnois, F. Montmessin, and F. Forget (2004), Three-dimensional modeling of ozone on Mars, *J. Geophys. Res.*, *109*, E07004, doi:10.1029/2004JE002268.

Molina, L. T., and M. J. Molina (1986), Absolute absorption cross sections of ozone in the 185- to 350-nm wavelength range, *J. Geophys. Res.*, *91*, 14,501–14,508.

Montmessin, F., F. Forget, P. Rannou, M. Cabane, and R. M. Haberle (2004), Origin and role of water ice clouds in the Martian water cycle as inferred from a general circulation model, *J. Geophys. Res.*, *109*, E10004, doi:10.1029/2004JE002284.

Montmessin, F., E. Quémerais, J. L. Bertaux, O. Korablev, P. Rannou, and S. Lebonnois (2006), Stellar occultations at UV wavelengths by the SPICAM instrument: Retrieval and analysis of Martian haze profiles, *J. Geophys. Res.*, *111*, E09S09, doi:10.1029/2005JE002662.

Novak, R. E., M. J. Mumma, M. A. DiSanti, N. Dello Russo, and K. Magee-Sauer (2002), Mapping of ozone and water in the atmosphere of Mars near the 1997 aphelion, *Icarus*, *158*, 14–23.

Noxon, J. F., W. A. Traub, N. P. Carleton, and P. Connes (1976), Detection of O_2 dayglow emission from Mars and the Martian ozone abundance, *Astrophys. J.*, *207*, 1025–1035.

Ockert-Bell, M. E., and J. F. Bell (1997), Absorption and scattering properties of the Martian dust in the solar wavelengths, *J. Geophys. Res.*, *102*, 9039–9050.

Parkinson, W. H., J. Rufus, and K. Yoshino (2003), Absolute cross section measurements of CO_2 in the wavelength region 163–200 nm and the temperature dependence, *Chem. Phys.*, *219*, 45–57.

Pollack, J. B., R. M. Haberle, J. Schaeffer, and H. Lee (1990), Simulations of the general circulation of the Martian atmosphere: 1. Polar processes, *J. Geophys. Res.*, *95*, 1447–1473.

Sander, S. P., et al. (2003), Chemical kinetics and photochemical data for use in atmospheric studies, Evaluation number 14, JPL Publ. 02-25, Jet Propul. Lab., Padadena, Calif.

Smith, M. D. (2002), The annual cycle of water vapor on Mars as observed by the Thermal Emission Spectrometer, *J. Geophys. Res.*, *107*(E11), 5115, doi:10.1029/2001JE001522.

Thuillier, G., M. Hersé, D. Labs, T. Foujols, W. Peetermans, D. Gillotay, P. C. Simon, and H. Mandel (2003), The solar spectral irradiance from 200 to 2400 nm as measured by the SOLSPEC spectrometer from the Atlas and Eureca missions, *Sol. Phys.*, *214*, 1–22.

Traub, W. A., N. P. Carleton, P. Connes, and J. F. Noxon (1979), The latitude variation of O_2 dayglow and O_3 abundance on Mars, *Astrophys. J.*, *229*, 846–850.

Wherbein, W. M., C. W. Hord, and C. A. Barth (1979), Mariner 9 ultraviolet spectrometer experiment: Vertical distribution of ozone on Mars, *Icarus*, *38*, 288–299.

World Meteorological Organization (1986), Atmospheric ozone: 1985, *WMO Rep. 16*, World Meteorol. Organ., Geneva.

J. L. Bertaux, F. Lefèvre, F. Montmessin, and S. Perrier, Service d'Aéronomie, Route des Gatines, BP 3, F-91371 Verrières le Buisson Cedex, France. (severine.perrier@aerov.jussieu.fr)

A. Fedorova and O. Korablev, Space Research Institute (IKI), 84/32 Profsovuznava, 117810 Moscow, Russia.

S. Lebonnois, Laboratoire de Météorologie Dynamique, IPSL, CNRS/UPMC, Box 99, F-75252 Paris Cedex 05, France.